Original Paper

Landslides
DOI 10.1007/s10346-017-0911-y
Received: 6 June 2017
Accepted: 20 October 2017
© Springer-Verlag GmbH Germany 2017

B. Matasci · G. M. Stock · M. Jaboyedoff · D. Carrea · B. D. Collins · A. Guérin · G. Matasci · L. Ravanel

Assessing rockfall susceptibility in steep and overhanging slopes using three-dimensional analysis of failure mechanisms

Abstract Rockfalls strongly influence the evolution of steep rocky landscapes and represent a significant hazard in mountainous areas. Defining the most probable future rockfall source areas is of primary importance for both geomorphological investigations and hazard assessment. Thus, a need exists to understand which areas of a steep cliff are more likely to be affected by a rockfall. An important analytical gap exists between regional rockfall susceptibility studies and block-specific geomechanical calculations. Here we present methods for quantifying rockfall susceptibility at the cliff scale, which is suitable for sub-regional hazard assessment (hundreds to thousands of square meters). Our methods use three-dimensional point clouds acquired by terrestrial laser scanning to quantify the fracture patterns and compute failure mechanisms for planar, wedge, and toppling failures on vertical and overhanging rock walls. As a part of this work, we developed a rockfall susceptibility index for each type of failure mechanism according to the interaction between the discontinuities and the local cliff orientation. The susceptibility for slope parallel exfoliation-type failures, which are generally hard to identify, is partly captured by planar and toppling susceptibility indexes. We tested the methods for detecting the most susceptible rockfall source areas on two famously steep landscapes, Yosemite Valley (California, USA) and the Drus in the Mont-Blanc massif (France). Our rockfall susceptibility models show good correspondence with active rockfall sources. The methods offer new tools for investigating rockfall hazard and improving our understanding of rockfall processes.

Keywords Rock mass · Slope stability · Exfoliation failure · Terrestrial laser scanner · Yosemite Valley · The Drus

Introduction

The evolution of steep rocky landscapes is strongly influenced by the occurrence of rockfalls (Varnes 1978; Selby 1982; Matsuoka and Sakai 1999; Hungr et al. 1999; Hales and Roering 2007; Moore et al. 2009; Stock and Uhrhammer 2010; Barlow et al. 2012). However, predicting locations where future rockfalls will occur remains challenging and speculative. Rosser et al. (2007), Abellan et al. (2010), and Royan et al. (2014) demonstrated the possibility of forecasting rockfalls according to precursory deformation, but often, such deformation is either not present or not detectable prior to failure, especially in strong rocks such as granite. Assessing rockfall hazard requires knowledge of which areas are exposed to the impacts of rock blocks below unstable cliffs (Einstein 1988; Evans and Hungr 1993; Crosta and Agliardi 2003; Dorren and Seijmonsbergen 2003; Guzzetti et al. 2003; Baillifard et al. 2003). Thus, accurate determination of the most likely rockfall source areas is of primary importance for reliable rockfall hazard assessment (Harp and Noble 1993; Mazzoccola and Hudson 1996; Aksoy and Ercanoglu 2006; Copons and Vilaplana 2008; Vangeon et al. 2001; Guzzetti et al. 2003; Wieczorek et al. 2008).

Two scales of analysis are commonly used to investigate rockfall susceptibility: regional studies that cover entire valleys or regions (areas of square kilometers) and block-specific studies that investigate the stability of a single rock compartment (areas of square meters). Regional studies are usually based on general morphological parameters, such as slope steepness, that are analyzed in GIS environments using aerial digital elevation models (DEMs) (Strahler 1954; Wieczorek and Snyder 1999; Guzzetti et al. 2003; Frattini et al. 2008; Loye et al. 2009; Michoud et al. 2012; Messenzehl et al. 2016). In contrast, block-specific geomechanical stability calculations can be applied only locally, using simplified topographies (Eberhardt 2003; Grenon and Hadjigeorgiou 2008; Gischig et al. 2011). The determination of the many detailed parameters necessary for geomechanical calculations requires extensive laboratory tests and fieldwork, which can be further hampered by dangerous field conditions. For the purposes of determining potential future rockfall sources from a cliff, regional studies tend not to be sufficiently accurate, and block-specific geomechanical studies are often too narrowly specific in their calculation and application to be more widely applicable. Thus, a critical gap exists between these two types of analysis, especially in large and overhanging cliffs with complex topography. Here we address this gap by developing and evaluating methods for quantifying rockfall susceptibility at the cliff scale (hundreds to thousands of square meters).

Rockfall susceptibility assessment

Rockfall potential and susceptibility at the cliff scale are strongly linked to slope morphology. Accordingly, detailed terrain models are critical for quantifying the activity of rockfall sources, estimating potential unstable volumes, and measuring the orientations of the main joint sets that serve to destabilize rock masses (Terzaghi 1962; Selby 1982; Dershowitz and Einstein 1988; Priest 1993; Irigaray et al. 2003; Ferrero et al. 2009; Stead and Wolter 2015). Terrestrial laser scanning (TLS) and photogrammetry data are particularly useful, as these ground-based techniques deliver high-resolution three-dimensional models of topography (Wickens and Barton 1971; Slob and Hack 2004; Collins and Sitar 2008; Oppikofer et al. 2008; Lato et al. 2009; Jaboyedoff et al. 2012; Abellan et al. 2014). Further, acquisition of ground-based data is mandatory when investigating overhanging areas, which are poorly resolved with airborne acquisitions (Paronuzzi and Serafini 2009; Tsesarsky and Hatzor 2009; Stock et al. 2011, 2012; Dunham et al. 2017). Moreover, photogrammetry performed with UAV can be useful to cover a gap between aerial and terrestrial techniques and thus

Published online: 09 November 2017

avoid hidden zones in terrain models (Niethammer et al. 2012; Nex and Remondino 2014).

Unstable rock compartments are a direct consequence of the arrangement of the discontinuities in a rock mass, so determining rockfall susceptibility typically begins by measuring the orientations of those discontinuities (Hudson and Priest 1983). Several methods exist to measure discontinuity orientations using terrestrial point clouds (Jaboyedoff et al. 2007; Gigli and Casagli 2011; Lato and Vöge 2012; Voege et al. 2013; Riquelme et al. 2014), and discontinuity spacing and trace length data can also be quantified on terrestrial point clouds (Lato et al. 2009; Sturzenegger and Stead 2009; Sturzenegger et al. 2011; Lato et al. 2012). The orientation of discontinuities relative to the slope surface then determines the potential failure mechanisms (Goodman and Bray 1976; Hoek and Bray 1981; Norrish and Wyllie 1996) and the probability of mobilization. This can be assessed by performing kinematic analyses on DEMs (Gokceoglu et al. 2000; Jaboyedoff et al. 2004; Guenther et al. 2004, 2012). The angle between the discontinuities and the slope, coupled with trace length and spacing measurements, was employed by Jaboyedoff et al. (2004) to calculate discontinuity density and the number of potential slope failures. These results allow identification of the most probable failure zones and form one possible input for rock slope hazard assessment (Baillifard et al. 2003; Jaboyedoff et al. 2009; Brideau et al. 2011). The calculation of the spatial distribution of failure mechanisms on a mesh acquired by terrestrial laser scanning was carried out by Fanti et al. (2013) with the objective of securing the stability of a cultural heritage site and by Gigli et al. (2012) to conveniently place trajectory profiles and accurately map the rockfall hazard. Dunham et al. (2017) developed a point cloud-derived approach for assessing rockfall hazard over large areas based on an index or rockfall activity. The current study has points in common with the works of Fanti et al. (2013), Gigli et al. (2012), and Dunham et al. (2017): the use of high-resolution 3D point clouds, the analysis of the failure mechanisms, and the investigation of overhanging slopes in order to improve the analysis of rockfall hazard. In addition, this paper proposes new methods to enhance the quantification of the susceptibility of a rock cliff area to produce rockfalls. We focus on the detection of those areas most susceptible to rockfalls driven by planar, wedge, and toppling failure, as well as exfoliation-type failure (surface parallel) (Hoek and Bray 1981) (Fig. 1). The methods applied are mainly based on the geometrical intersection of joint sets with cliff topography. We developed a routine to compute the failure mechanisms in three dimensions, adapting the kinematic tests to analyze rock mass stability also in overhanging areas. Our methodology begins with the treatment of high resolution ground-based light detection and ranging (LiDAR) point clouds to characterize the fracture patterns found in rock cliffs. Following these procedures, we use the geometrical information to perform a rockfall susceptibility assessment at the cliff scale based on the calculation of the spatial distribution of the main failure mechanisms. From the study of rockfall processes in the field and from the analysis of past events, we developed an index of susceptibility to failure for each type of mechanism. Here we apply our methodology to two famously steep landscapes with known rockfall hazard: Glacier Point cliff in Yosemite Valley, California, USA (Wieczorek and Snyder 1999; Wieczorek et al. 2008; Stock et al. 2011, 2012, 2013) and the west face of the Drus on the Mont Blanc massif, France (Deline et al. 2006; Ravanel and Deline 2008, 2011; Ravanel et al. 2010; Matasci et al. 2015; Guérin et al. 2017).

Data acquisition and treatment

Our methodology for estimating rockfall susceptibility is by its nature a data-dependent process. In the methodology and model validation presented herein, we use data from our two case studies (Glacier Point in Yosemite Valley, USA and the west face of the Drus in the Mont-Blanc massif, France). Additional details for each of these study areas are provided in subsequent sections (Figs. 6 and 10).

Terrestrial laser scanning

For collection of high-resolution LiDAR data, we used an Optech Ilris LR laser scanner at each study area to obtain point clouds with a mean point spacing of 10 cm (Table 1). We then aligned the different ground-based scans together with an Iterative Closest Point (ICP) algorithm (Besl and Mckay, 1992; Chen and Medioni 1992) to obtain a complete point cloud of each study area. The point clouds were georeferenced through alignment with 1 × 1 m cell size aerial laser scanning (ALS) DEMs using identical ICP algorithms as used for registration (Slob and Hack 2004; Stock et al. 2011; Jaboyedoff et al. 2012; Abellan et al. 2014).

High-resolution photography

To color the point cloud data and sharpen the detail of the resultant TLS meshes, we acquired high-resolution panoramic photographs using a GigaPan robotic camera mount (Stock et al. 2011) with a Canon 5D camera body and a 300-mm lens. In this method, hundreds of photographs are taken automatically following a grid and then stitched together with the GigaPan software to create a several gigapixel-sized image. From these panoramic images, it is possible to extract high-resolution close-up images to observe meter-scale details in high definition. Moreover, we subsequently draped these photographs on the mesh of TLS point clouds at each study area to obtain accurate 3D models of the rock surface (Fig. 1c). This step was performed with 3DReshaper software. The textured models are very useful to map joint sets, identify rockfall scars, and compute rockfall volumes.

Methods

Characterizing fracture patterns

Joint orientations

Rockfall susceptibility is highly influenced by the orientations of discontinuities such as joints, faults, bedding planes, and geologic contacts (Goodman and Bray 1976; Hudson and Priest 1983; Stead and Wolter 2015). In our study areas, the primary discontinuities are joints, and hereafter, we deal only with joint orientations. We used Coltop3D software (Jaboyedoff et al. 2007) to measure the orientation of the joints from the point cloud data and to obtain a distinct point cloud sub-grouping for each joint set (Fig. 2a). The software computes the spatial orientation (dip direction and dip) of each point within a point cloud with respect to its neighboring points. It attributes a unique RGB color to each spatial orientation, allowing accurate identification of the major joint sets. Applied to dense 3D point

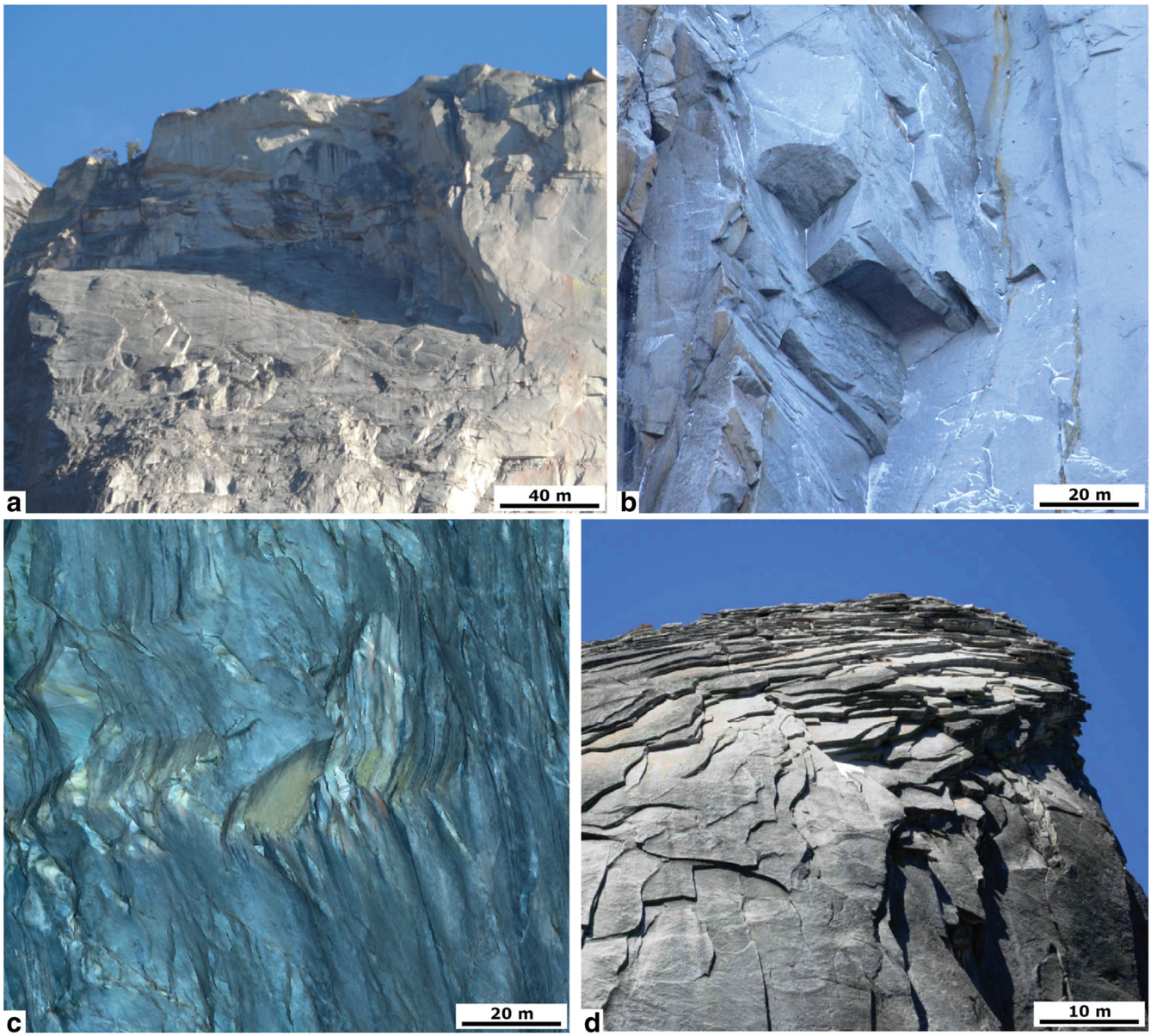

Fig. 1 Examples of cliff-scale failure mechanisms. **a** Planar failure scar in Yosemite Valley. **b** Steep wedge failures on the west face of the Drus (Mont-Blanc massif). **c** Textured TLS point cloud mesh of part of Glacier Point cliff (Yosemite Valley) showing steep discontinuities dipping inside the rock mass and susceptible to toppling detachments. **d** Pervasive exfoliation joints sub-parallel to the topographic slope in Yosemite Valley

clouds, Coltop3D allows for rapid identification of joint sets and measurement of their orientations (Oppikofer et al. 2011; Humair et al. 2013). The mean value of each joint set can be determined with high accuracy using density stereographic projections. We used field observations and examination of high-resolution photographs to ensure that our structural measurements were made on discontinuity-controlled bedrock surfaces (Fig. 2b), as opposed to soil or talus-covered slopes or erosion surfaces with little or no structural relevance. Traditional field surveys (e.g., using a Brunton-type compass) were essential for validating the orientation and the characterization of the joint sets measured remotely.

Table 1 Terrestrial laser scanning acquisitions

	Terrestrial laser scanning Number of scan points	Number of scans	Distance to the slope (m)	Angle of scanning (°)
The Drus	3	5	300–1000	10–30
Glacier Point	3	3	500–1500	10–20

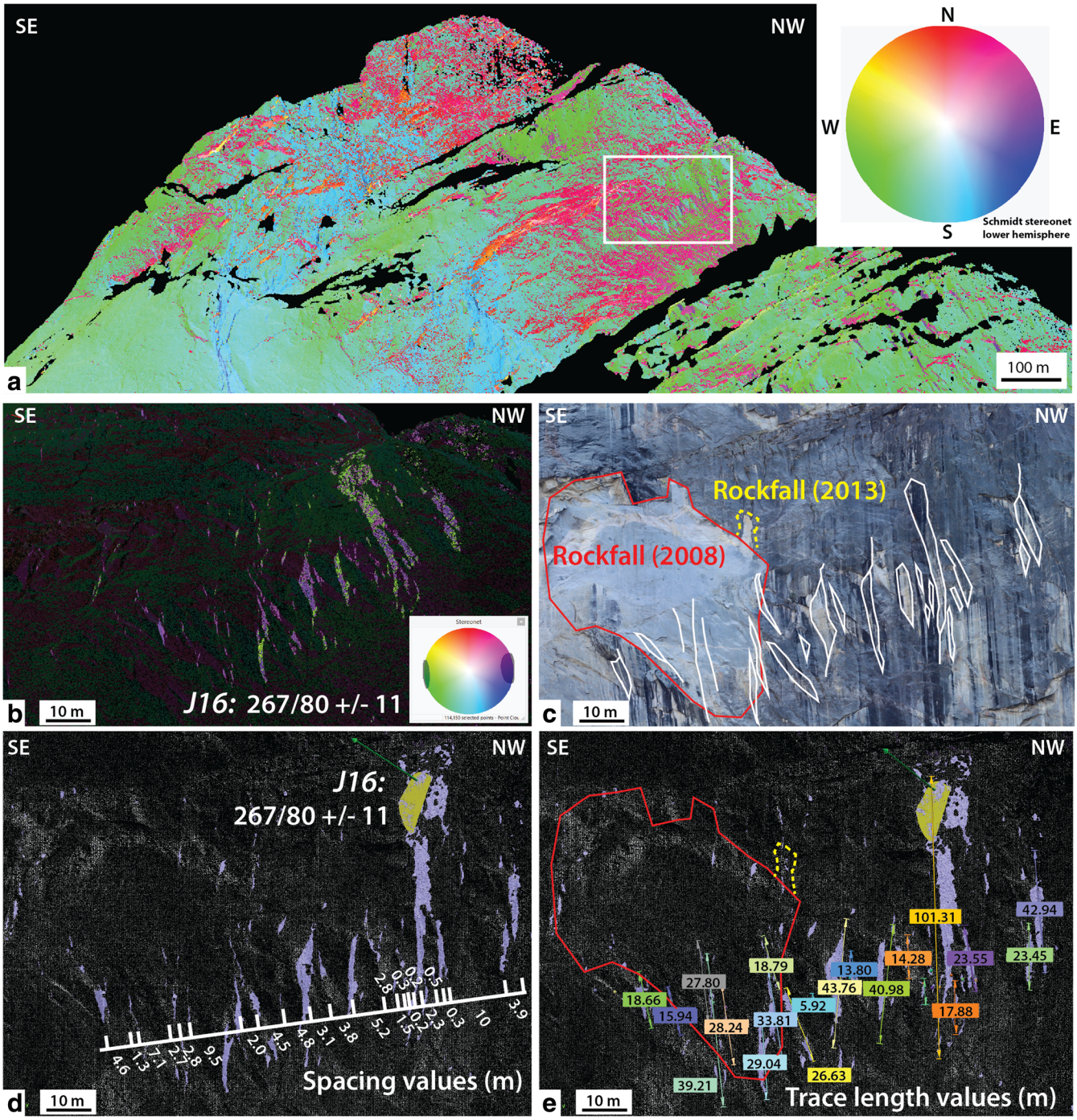

Fig. 2 **a** Visualization of the TLS point cloud of the northeast face of Glacier Point (Yosemite Valley). The point cloud is colored according to the orientation of the poles of the points (stereographic projection). The white box highlights the close-up displayed in b–e where rockfalls occurred in 2008 (Stock et al. 2011) and 2013. **b** Selection of points showing joint set J16. The stereographic projection displays the poles in a Schmidt stereoplot, lower hemisphere and equal area. **c** High-resolution photograph of the same area as **b**. The planes or the traces of J16 are contoured in white. **d** Joint spacing measurements for J16 (violet areas) along a profile. **e** Joint trace length measurement on a point cloud colorized by joint orientation

Spacing of joint sets

To measure joint set spacing, we selected the points of a point cloud that correspond to an individual discontinuity set. For example, Fig. 2b shows the selection of points related to joint set J16 in the Glacier Point cliff in Yosemite Valley. These points were investigated to measure set spacing along scanline profiles (ISRM 1978) (Fig. 2d). This procedure requires constructing a plane according to the mean orientation of the set and calculating the normal vector to the set. Along a cross section on the TLS data, we then anchored a point at every joint. Subsequently, at every

anchored point, we created a plane parallel to the orientation of the mean value of the set. These planes were constructed with the orientation of the normal vector and with the coordinates of the point. Then, the equation of each plane was exported and eventually the distance between the planes calculated. We applied this process to every joint set along several cross sections, providing the mean spacing of each set within the rock mass.

Trace length of joint sets

To obtain joint set trace length, we measured the delineated joint sets previously identified by the joint set spacing analyses (Fig. 2d) via manual inspection in our point cloud processing software. We used TLS meshes textured with GigaPan photographs to accurately follow the traces of the joints, even where discontinuity planes do not outcrop and only a fracture is visible (Fig. 2e). We performed dozens of measurements for every joint set along several scanline profiles according to standardized statistical protocols (ISRM 1978; Sturzenegger et al. 2011).

Analysis of failure mechanisms

We identified potential unstable slope areas in the point clouds with a routine based on finding the intersection between the orientation of the joint sets and the cliff topography. This calculation allows visualizing how many potential failure mechanisms are possible in every part of the cliff (see subsequent sections). As this initial analysis is only based on the existence of intersections at the surface, it can be greatly refined for the rock mass as a whole by considering additional parameters such as the joint set spacing, joint set trace length, and the angles between the topography and the joint sets ("Final rockfall susceptibility" section). In theory, a given geometrical configuration can produce a failure, but in reality, it may also be very unlikely to occur, for example, because of the low steepness of the joint (Goodman and Shi 1985; Jaboyedoff et al. 2004). Thus, we developed specific equations to calculate an index of susceptibility for each type of failure (described subsequently). To ensure accuracy in the calculations, we tested every step of the routine with a synthetic point cloud composed of a quarter of a sphere displaying several facets with different orientations (Fig. 3).

Identification of potential failure areas

Following earlier work (Markland 1972; Hoek and Bray 1981; Goodman and Shi 1985; Romana 1993; Norrish and Wyllie 1996), we used the equations of kinematic tests to extract points where planar, wedge, or toppling failure is geometrically possible in our topographic models. By using ground-based TLS data to create 3D models, we are able to compute failure mechanisms in overhanging areas as well, which are not possible using airborne-based ALS data and DEM-based software packages alone. Using Coltopo3D software, we calculated the normal vector to every point of the topography based on a mean number of ten neighbors (Jaboyedoff et al. 2007). The choice of number of neighbors depends on the density of the point cloud and the roughness of the cliff (frequency of fractures) (Jaboyedoff et al. 2007). The normal vectors (pole) are in the format *dx*—easting, *dy*—northing, and *dz*—positive, resulting in vectors directed always upward. However, to perform kinematic failure analysis, it is necessary to know which areas of a 3D model are overhanging and with consequentially actual normal vectors facing downward (i.e., facing the ground). To define these areas, we calculated a vector between the acquisition device and every point of the scan. We then determined the scalar product between this vector and the pole of the topography. When the result is negative, the two vectors cannot be located in the same half-sphere and thus are pointing in opposite directions. In these cases, the normal vector was inverted, resulting in a negative *dz* component that thereby identifies the overhanging areas of the cliff (Fig. 3d). Subsequently, we calculated the dip direction and dip (slope angle) of every point based on the three components of the normal vector (Eqs. 1 and 2; Fig. 3b, c):

$$\text{Dip } \textit{direction} = \left[360 - \arctan^2(dy, dx)\frac{180}{\pi}\right] + 90 \tag{1}$$

$$\text{Dip} = \arccos(dz)\frac{180}{\pi} \tag{2}$$

where dip direction and dip are in degrees and (*dx*, *dy*, *dz*) is the normal vector (pole) of the slope. Moreover, when $dz < 0$, the point is located in an overhanging area and thus, the result of Eq. 1 must be increased by 180°.

In developing the equations for each of the failure mechanisms derived in the subsequent sections, normal slope refers to those areas of the cliff that have a dip direction toward the laser scanner and have positive *dz* component of the pole, whereas overhanging slopes are those that dip in the opposite direction, namely into the cliff, and have negative *dz* (Fig. 3d).

Planar failure Two conditions must be satisfied for planar failure on normal slopes ($dz > 0$) (Bieniawski 1973, 1979; Romana 1985, 1993; Wyllie and Mah 2004):

$$\alpha_i - t < \alpha_p < \alpha_i + t \tag{3}$$

and

$$\beta_i < \beta_p \tag{4}$$

where α_i is the dip direction of a joint set *i*, α_p is the dip direction of a given point *P*, β_i is the slope angle of a joint *i*, β_p is the slope angle of the topography at a given point *P*, and *t* is the tolerance of the dip direction (to account for statistical distributions of joint measurements). In our case study analyses, we use a value of *t* equal to 20°.

For overhanging areas (i.e., non-normal slopes, $dz < 0$), only one condition is required because there is no need to restrain the conditions according to the slope steepness (Fig. 4a):

$$(180 + \alpha_i) - t < \alpha_p < (180 + \alpha_i) + t \tag{5}$$

The first loop of the routine verifies which points of the 3D point cloud satisfy these requirements to potentially host a planar failure according to the characteristics of the first joint set. Additional loops repeat the task for the other joint sets.

Wedge failure A wedge failure is defined by two joints, herein labeled *i* and *j*. The intersection line formed by the two joints is the wedge axis and is characterized by its trend (α_{ij}) and plunge (β_{ij}). Similar to planar failure, points where wedge failure can exist must satisfy individual conditions for normal and overhanging slopes

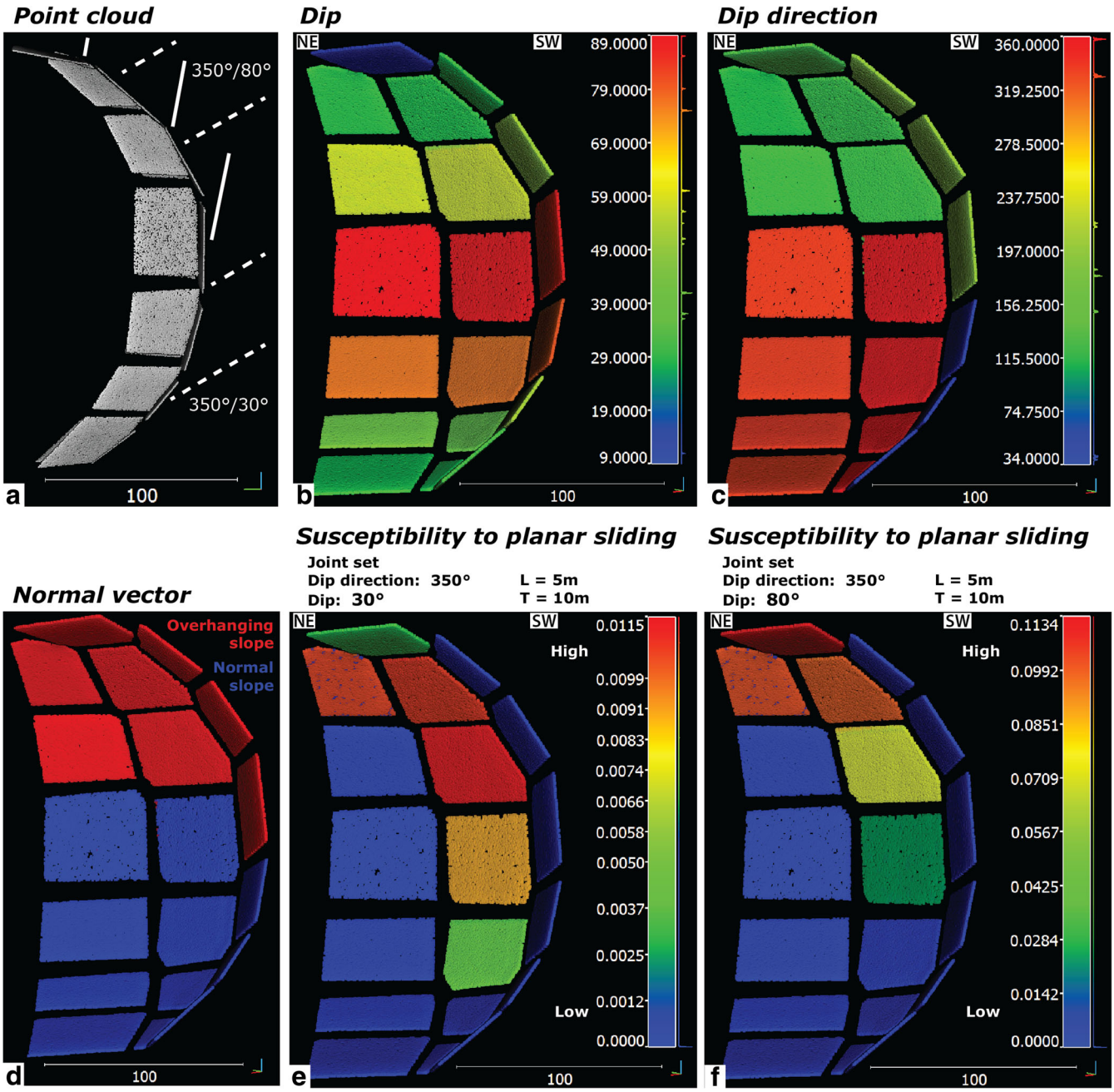

Fig. 3 Calculations on a synthetic quarter of a sphere point cloud. **a** Cross section of the synthetic point cloud. The white dotted lines show a shallow joint set oriented at 350°/30°, used for the calculations displayed in **e**. The white lines show a steep joint set oriented at 350°/80°, used for the calculations displayed in **f**. **b** and **c** display, respectively, an oblique view of the dip and dip direction of the points. **d** Orientation of the normal vector (pole) of each point. Blue areas represent normal slopes (pole facing up, $N_z > 0$), whereas red areas correspond to overhangs (pole facing down, $N_z < 0$). **e** Map of susceptibility to planar failure for a joint set oriented 350°/30°. **f** Map of susceptibility to planar failure for a joint set oriented 350°/80°. In this example, the steeper joint set results in a higher susceptibility index in the overhanging part of the synthetic point cloud

(Bieniawski 1973, 1979; Romana 1985, 1993; Wyllie and Mah 2004) (Fig. 4a). For normal slopes ($dz > 0$):

$$\alpha_{ij} - t < \alpha_p < \alpha_{ij} + t \tag{6}$$

and

$$\beta_{ij} < \beta_p \tag{7}$$

For overhanging slopes ($dz < 0$):

$$(180 + \alpha_{ij}) - t < \alpha_p < (180 + \alpha_{ij}) + t \tag{8}$$

where α_p is the dip direction and β_p is the slope angle, respectively, of a given point *P*. *N* combinations are possible to form a wedge with *n* joint sets, such that

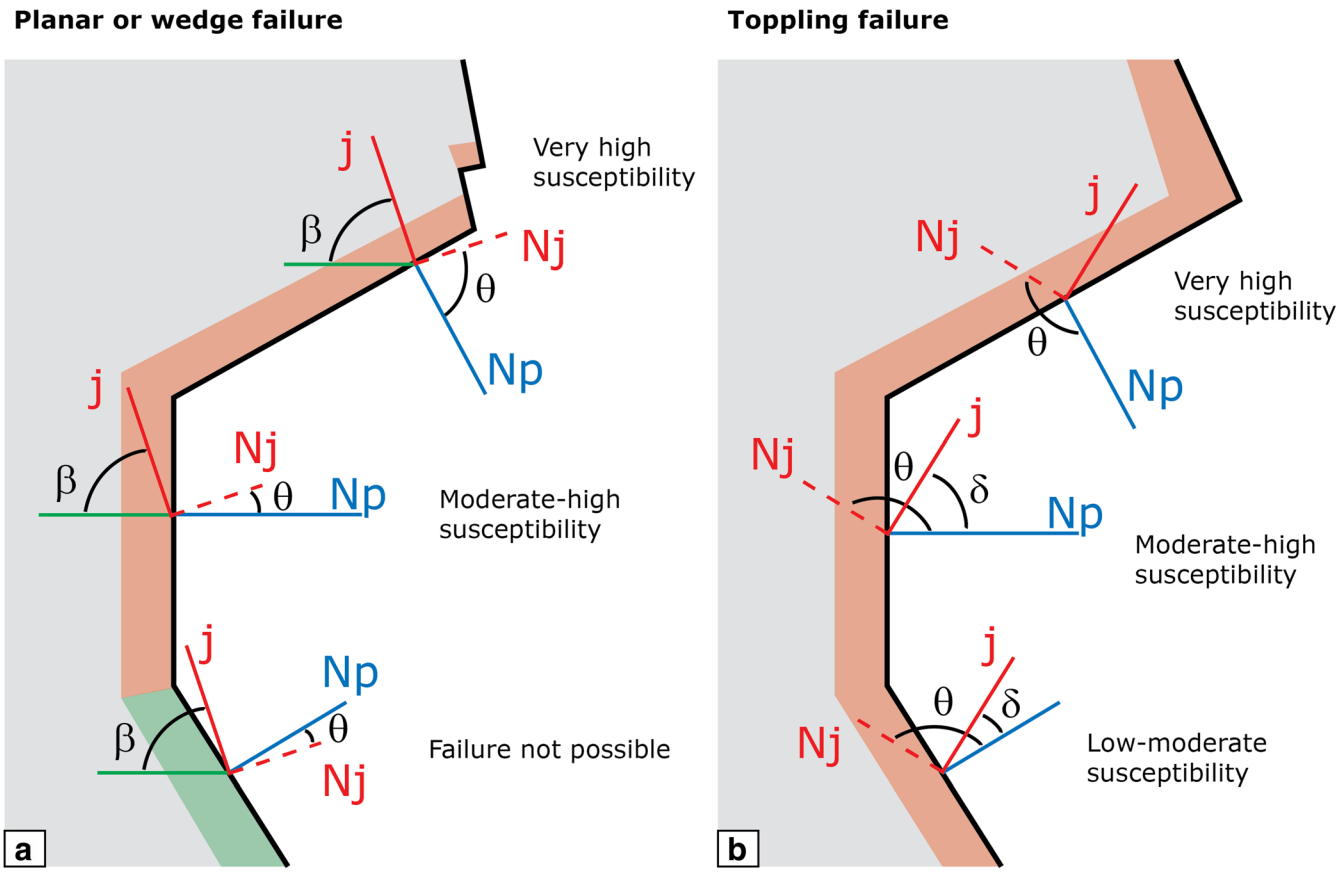

Fig. 4 **a** Two-dimensional representation of potentially unstable areas for planar failure according to joint set *j*. N_j is the normal vector (pole) to the joint *j*. N_p is the normal vector to the topography at the point *P*. The image **a** is the same for wedge failure, by considering *j* as the intersection line between two discontinuities rather than only a joint plane. Red shading represents the areas where a failure is possible, whereas the green shading highlights the stable part of the slope. **b** Two-dimensional representation of the potential unstable areas for toppling detachment. For both planar and toppling detachments, overhangs are areas of very high rockfall susceptibility

$$N = \frac{n(n-1)}{2} \tag{9}$$

Numerical loops are performed in the routine to verify the possibility of failure of each combination of joint sets in every point of the point cloud.

Toppling detachment The point *P* where a toppling failure mode is possible must also satisfy geometric conditions for values of the dip direction (α_i) and dip (β_i) of joint sets (Bieniawski 1973, 1979; Romana 1985, 1993; Wyllie and Mah 2004) (Fig. 4b). For normal slopes ($dz > 0$):

$$(\alpha_i + 180) - t < \alpha_p < (\alpha_i + 180) + t \tag{10}$$

and

$$90 - \beta_i \leq \beta_p \tag{11}$$

For overhanging slopes ($dz < 0$):

$$\alpha_i - t < \alpha_p < \alpha_i + t \tag{12}$$

where α_p and β_p are the dip direction and dip, respectively, of a given point *P*. As previously, we used a tolerance *t* equal to 20° in our case study analyses. The calculation loop is repeated for every joint set from 1 to *i*.

At this point, we know the areas where a given joint set (or couple of joints, for wedge failures) can produce a failure according to one of the three mechanisms.

Failure susceptibility index

The previous calculations provide an indication of whether or not a particular failure mechanism is possible. However, for quantitative rock fall hazard analysis, we must also calculate the susceptibility when one of those failure mechanisms is geometrically possible (i.e., there is a positive result to one of the calculation loops described previously for planar, wedge, or toppling). We therefore calculated a susceptibility index based on the average surface that every joint set (or combinations of two joint sets in the case of wedge failure) forms on the topography according to its spacing, trace length, and incidence angle (Jaboyedoff et al. 1996, 2004). The susceptibility index also depends on the steepness of the joint set (or of the intersection line in the case of wedge failure) and finally defines the slope areas with the most favorable orientations for overall failure from the three mechanisms combined.

Planar failure We evaluate the potential for planar failure by calculating, with the scalar product, the incidence angle θ between the normal vector d_P to the topography at point P, and the normal vector D_i to joint set i:

$$\theta = \arccos(d_P D_i) \tag{13}$$

Then, we define the susceptibility to planar failures S_p related to the joint set i, in the point P, by

$$S_p = A\frac{\sin(\theta)}{LT}\tan\beta_i \tag{14}$$

where θ is the angle between the normal vector to point P and the normal vector to joint set i, L and T are respectively the average spacing and trace length of the joint set i, and β_i is the mean slope angle of joint set I (Fig. 3e). The calculation of S_p can be standardized by using a standard area, A, equal to 1 m².

Wedge failure We evaluate the potential for wedge failure by calculating at every point P the density of wedges (N_w) based on the average spacing values (L_i and L_j) of the two joint sets, an area A of 1 m², the angle γ between the two sets, and the angle λ between the wedge axis and the pole of the topography (point P) (Jaboyedoff et al. 1996, 2004):

$$N_w = A\frac{\cos(\lambda)\sin(\gamma)}{(L_i L_j)} \tag{15}$$

This value of N_w is valid when the joint sets are fully persistent, which is rarely the case. For this reason, N_w must be multiplied by a factor p that accounts for the probability that joint sets i and j intersect to form a wedge. To calculate p, it is necessary to know the apparent spacing $Lapp$ of the first joint set along the trace T of the second joint set (Jaboyedoff et al. 1996):

$$Lapp_i = \frac{L_i}{\sin\gamma} \tag{16}$$

$$p = \frac{T_i \quad T_j}{Lapp_j \, Lapp_i} \tag{17}$$

The susceptibility to wedge failure depends on the steepness of the wedge axis and on the K factor. The K factor integrates the effect of the opening of the wedge and of the angles between each joint set and the horizontal plane (Wyllie and Mah 2004).

$$K = \frac{\sin\alpha_i + \sin\alpha_j}{\sin(\alpha_i + \alpha_j)} \tag{18}$$

where α_i and α_j are the angles between the horizontal plane and the joint set i or j, respectively. Thus, in a given point P, the susceptibility to wedge failure S_w, formed by the sets of joints i and j would be

$$S_w = N_w \;\; P\frac{\tan\beta_{ij}}{K} \tag{19}$$

where β_{ij} is the plunge of the line of intersection of planes i and j (Fig. 3f).

Toppling detachment We suggest a susceptibility index for toppling detachment in the normal slopes proportional to the steepness of the joint set. Conversely, in the overhanging areas, the susceptibility to toppling detachment is greater where the topography is sub-parallel to the relevant joint set. For normal slopes ($dz > 0$):

$$S_t = A\frac{\sin(\theta)}{LT}\tan(\delta) \tag{20}$$

and for overhanging slopes ($dz < 0$):

$$S_t = \frac{A}{LT}\frac{1}{\tan(\theta)} \tag{21}$$

where θ is the angle between the normal vector to point P and the normal vector to joint set i, L and T are respectively the spacing and the trace length of the joint set i, A is an area of 1 m², and $\delta = \theta - 90°$.

Final rockfall susceptibility

For each point of the point clouds, we can calculate the sum of the susceptibility indexes obtained for the joint set calculation loops of the three mechanisms. The final result S_{tot}, representing the best estimation of the failure susceptibility for a given point P, is the sum of the indexes of all the planar (S_p), wedge (S_w), and toppling (S_t) potential failures at that point:

$$S_{tot} = \sum S_p + \sum S_w + \sum S_t \tag{22}$$

Whereas this calculation provides a numerical value of susceptibility, the classification of low or high susceptibility must be analyzed relative to each individual cliff face. Further, it should be noted that the resultant susceptibility does not identify that a failure will occur (e.g., that the rock friction angle is less than the slope angle for planar failure), but rather that cliff-scale rock compartments are more or less susceptible to failure based on their geometry alone when compared to other rock compartments along the cliff.

Exfoliation failures

Many rock masses are susceptible to exfoliation-type joint failure, whereby failure can occur along joints that are oriented subparallel to the cliff face with only infrequent daylighting (joint intersection) with the topographic surface. This is true at both of the case studies investigated herein (Yosemite Valley and the Drus) where exfoliation is common in the granitic rock masses that form their respective steep landscapes (Bahat et al. 1999; Martel 2006, 2011; Stock et al. 2012; Leith et al. 2014; Collins and Stock 2016). We observed that the detachment surfaces for many historical rockfalls in Glacier Point (Yosemite Valley) were along exfoliation joints and bounded by regional tectonic joints. Our susceptibility index for planar failure captures exfoliation when exfoliation joints are intersecting steep slopes or overhanging structures (Fig. 5). The topographic points constituting an overhang will

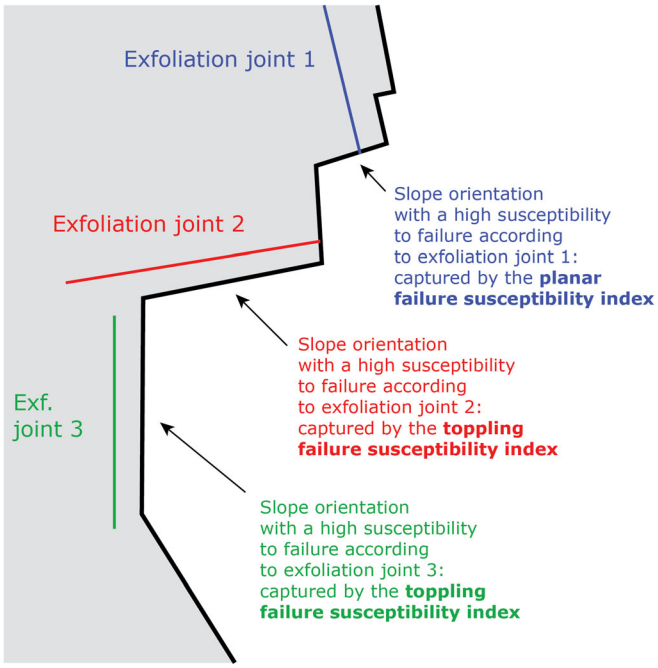

Fig. 5 Schematic two-dimensional representation of the contribution of exfoliation joints to rockfall susceptibility. The effect of a failure along an exfoliation joint is captured either by planar or by toppling susceptibility index, depending on the local confrontation between the orientation of the slope and the orientation of the exfoliation joint

display a particularly high susceptibility due to the exfoliation joint because it intersects that slope area almost perpendicularly (e.g., Figs. 1d, 4a, and 5). Toppling susceptibility index also captures part of exfoliation failures as this index is maximal when the joint set is parallel to the cliff face (Fig. 5). The points of the cliff that have the same orientation as a joint set will display a high toppling index and thus increase the overall rockfall susceptibility for that location. However, pure exfoliation failures, developing without the interaction with oblique tectonic joints, are difficult to resolve before a rockfall occurs because the exfoliation joints are essentially parallel to the cliff face and therefore most often hidden within the cliff.

Inventory of rockfall events

To validate our methods for quantifying rockfall susceptibility, we defined the locations of existing rockfall scars for our two study sites: the cliff below Glacier Point in Yosemite Valley and the west face of the Drus in the Mont-Blanc massif. For Yosemite Valley, we have a rich inventory database of rockfalls spanning over 150 years (Stock et al. 2013). At the Drus, Ravanel and Deline (2008) quantified rockfall activity by comparison of historical photographs over a period of about 100 years. In addition, we performed detailed annual TLS monitoring from 2010 to 2016 on the cliffs of Yosemite Valley and at the Drus, which detected several rockfall events, even of very small volumes (< 0.5 m^3).

Application 1: Glacier Point cliff (Yosemite Valley, California, USA)

Yosemite Valley is an east-west 11-km-long, ~ 1-km-deep valley cutting the western slope of the central Sierra Nevada mountain range in California, USA (Fig. 6). The glacially steepened cliffs experience numerous rockfalls each year (Stock et al. 2013), posing risk to the four million annual visitors to the park (Wieczorek and Snyder 1999; Wieczorek et al. 2008; Stock et al. 2011, 2012, 2013, 2014).

Geological setting and fracturing pattern

Yosemite Valley was carved by Pleistocene glaciations into Cretaceous age plutons of the Sierra Nevada batholith (Huber 1987; Bateman 1992; Calkins et al. 1985; Peck 2002). Exfoliation joints, formed (sub) parallel to topographic surfaces, are a characteristic feature of granitic rocks and are ubiquitous throughout the valley (Bahat et al. 1999; Wieczorek and Snyder 1999; Wieczorek et al. 2008; Martel 2006, 2011; Stock et al. 2011, 2012; Collins and Stock 2016) (Fig. 1d). The cliff beneath Glacier Point, located in the eastern portion of Yosemite Valley, is one of the tallest in Yosemite (about 800 m). The Glacier Point cliff is composed of Half Dome granodiorite in the lower part and Sentinel granodiorite in the upper part (Calkins et al. 1985). Using the methods previously described, we identified and characterized 16 different joint sets at Glacier Point (Table 2).

The value of 2σ is the double standard deviation. Joint sets with numbers not shown (J_1, J_3, J_4, etc.) do not consistently outcrop on the north facing exposure of the cliff.

Results

Our analysis for Glacier Point highlights the complex and sometimes overhanging topography of the cliff (Fig. 7a). In analyzing rockfall susceptibility, we colored the 3D points according to the value of the sum for each joint set, of the planar (Fig. 7b), wedge (Fig. 7c), and toppling (Fig. 7d) failure susceptibility indexes. Here, we find that the susceptibility of planar failure and

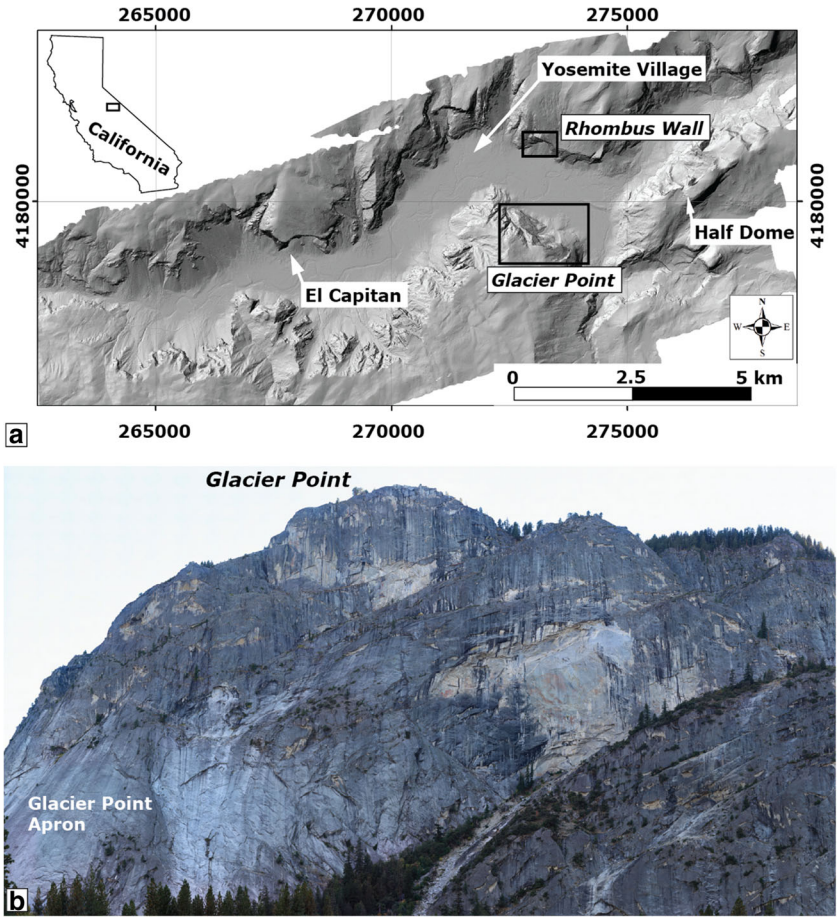

Fig. 6 **a** Aerial DEM of Yosemite Valley showing Glacier Point and the Rhombus Wall in the black boxes. The Porcelain Wall is located just left (west) of the summit of Half Dome. **b** Photograph of the northeast face of the Glacier Point cliff. The Glacier Point Apron is located in the lower eastern portion of the cliff

toppling detachment are similar, but generally low, with the index of the slope areas most likely to experience these kinds of failure reaching 0.05. However, some slope orientations are particularly favorable for the development of wedge failures and thus the susceptibility index for this mechanism reaches considerably higher values (up to 0.34) (Fig. 7c). We investigate susceptibility further by plotting the numbers of points within the point cloud where a joint set or a combination of joint sets can lead to a failure (Fig. 8a–c) and by computing the individual failure mode susceptibility over the point cloud (Fig. 8d–f). Some joint sets can theoretically lead to failures, but their spatial probability of occurrence is low, resulting in a small susceptibility index. For example, joint set J27 forms the highest number of points where planar failure is possible (Fig. 8a), but because it has a medium dip angle (56°), it has a reduced susceptibility index (Fig. 8d). In contrast, joint set J10 is ranked third in terms of numbers of potential planar failure points (Fig. 8a) but has the greatest sum of susceptibility indexes over the whole point cloud of the Glacier Point cliff (Fig. 8d), mostly because joint set J10 is very steep and oriented perpendicular to roof structures. J10 is also very persistent and represents one of the most important joints shaping the Glacier Point cliff. Several recent (1998 to present) rockfalls from the Glacier Point cliff have been associated with joint set J10, which is often parallel to the cliff face and thus locally considered as an exfoliation joint. The largest of these recent rockfalls associated with J10 is the October 2008 rockfall (5663 ± 36 m^3; Stock et al. 2011). Although J27 and J30 have lower susceptibility values than J10, they are important because they furnish a surface for planar failure of large rock masses.

With 16 joint sets, the number of theoretically possible wedges is 120 (Eq. 9), but only some are capable of daylighting at Glacier Point cliff, as illustrated in Fig. 9b. Those that have a significant susceptibility rating are even fewer; in particular, we note the combinations of 12–27, 12–30, 10–12, 7–12, 2–9, and 28–30 (Fig. 8e).

The most important joint set in terms of potential toppling detachment at the Glacier Point cliff is J31 (Fig. 8c). In fact, its orientation (223/69) is the opposite of the average dip direction of the cliff (030/75) leading to a high number of points prone to this type of failure (Fig. 8f).

Ultimately, the final rockfall susceptibility, obtained by summing the indexes for the different mechanisms (Eq. 22), can be compared to visible rockfall areas (in the form of rockfall scars) and to the inventory of historical events, which is significantly detailed in this area of Yosemite Valley (Stock et al. 2013). Rockfall areas active over the past few decades are located in zones determined to have relatively high susceptibility to rockfalls (Fig. 9).

Table 2 Summary of the main joint sets detected in the cliff below Glacier Point

Joint set	Dip direction (°)	Dip (°)	2σ (°)	Spacing (m)	Trace length (m)
J2	089	35	20	12	140
J5	250	35	17	18	81
J7	050	79	18	10	66
J8	118	51	13	16	77
J9	306	51	15	3	29
J10	011	85	12	4	55
J11	155	87	10	9	31
J12	119	88	19	5	19
J13	177	40	14	18	36
J16	267	80	11	13	35
J17	160	58	17	17	50
J27	025	56	13	7	65
J28	295	74	12	9	35
J29	180	8	16	11	40
J30	355	49	14	6	39
J31	223	69	14	10	25

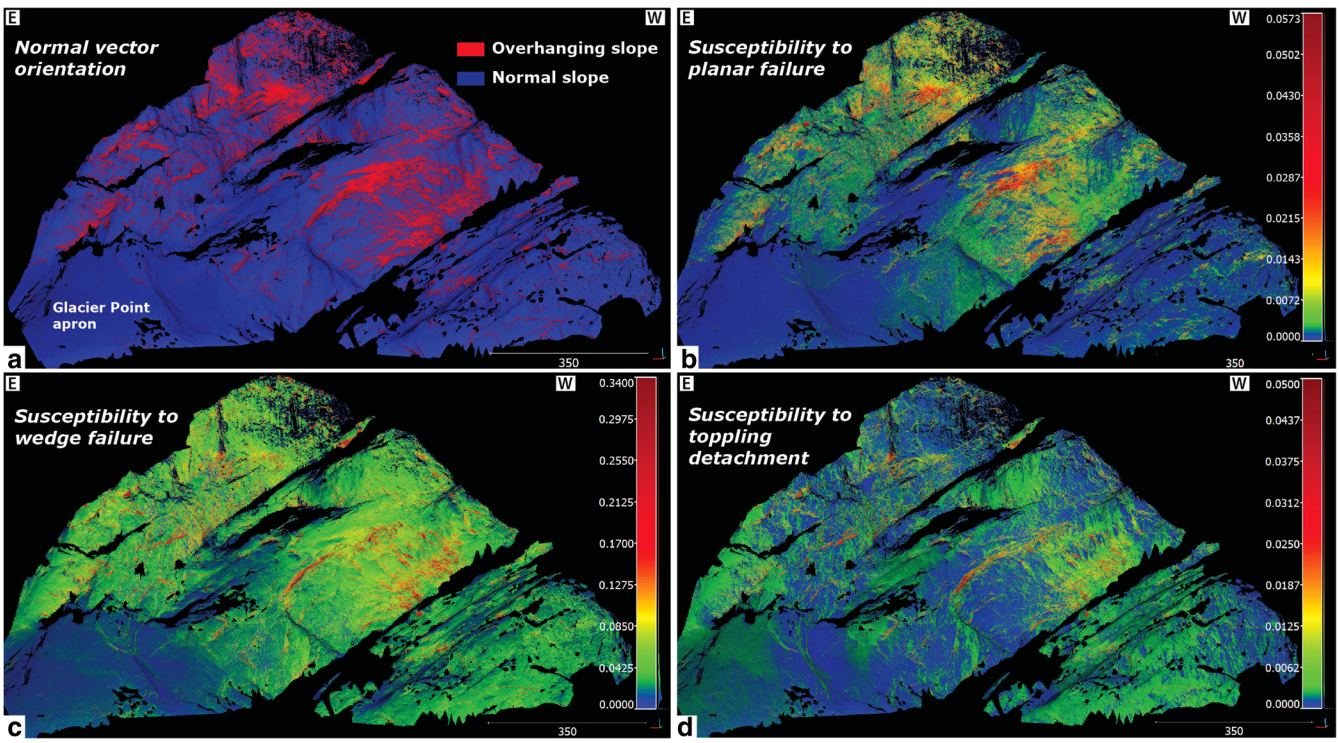

Fig. 7 Results for 2010 three-dimensional model of Glacier Point cliff in Yosemite Valley. **a** TLS point cloud showing overhanging areas in red. **b** Point cloud colored according to the sum of the planar failure susceptibility index for all 16 predominant joint sets (see Table 2). **c** Point cloud colored according to the sum of the wedge failure susceptibility index for all 120 combinations of joint sets. **d** Point cloud colored according to the sum of the toppling detachment susceptibility index for the detected joint sets

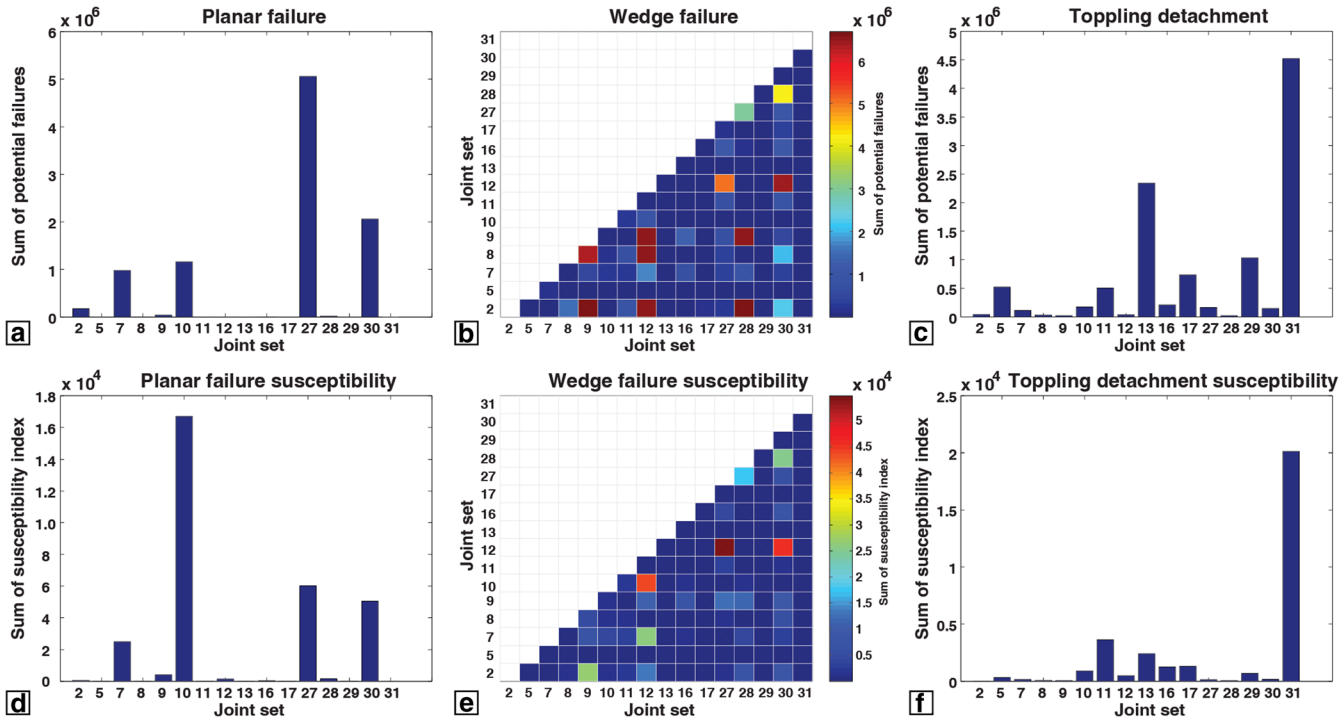

Fig. 8 Results of the failure mechanisms calculations for the Glacier Point cliff. **a**, **b**, and **c** display, respectively, the number of points where planar, wedge, or toppling failure can occur for each joint set or combination. **d**, **e**, and **f** display respectively the sum of susceptibility index for the points where planar, wedge, or toppling failure can occur for each joint set or combination

Application 2: the Drus west face (Mont-Blanc, France)

The Mont-Blanc massif is a mountain range about 40 km long and 10 km wide, located at the border of France, Italy, and Switzerland. It contains numerous sub-peaks and cliff faces, including the west face of the Drus (Fig. 10). Numerous rockfalls occurred in the twentieth century, and the evolution of this face is especially well documented by historical photographs (Ravanel and Deline 2008; Fig. 10c). During the last decade, this face was affected by several large rockfalls, most notably in the summer of 2005 (265,000 m^3; Ravanel and Deline 2008; Guérin et al. 2017) and in September (4532 ± 200 m^3) and October (54,731 ± 400 m^3) of 2011 (Matasci et al. 2015; Guérin et al. 2017) (Fig. 10b, c).

Geological setting and fracturing pattern

The Drus peaks are carved in the Mont-Blanc granitic batholith, which was intruded into the European gneissic basement (micaschists and gneiss) during the late Paleozoic Hercynian orogeny (Epard 1990; Bussy and Von Raumer 1994; Steck et al. 1999). Subsequent tectonic phases created several very steep and persistent joint sets within the rock mass. Using point clouds collected in both September 2010 and November 2011, we identified 14 different joint sets (Table 3) on the west face of the Drus.

Results

Rather than relating rockfall susceptibility for the entire cliff to a long-term rockfall inventory as we did for Yosemite, we performed temporally specific susceptibility analyses for several episodes of rock fall activity for the west face of the Drus. The bracketing dates of the point clouds collected for the west face of the Drus allowed us to perform specific "before and after" susceptibility assessments of a large pillar collapse (59,300 m^3) that occurred in September–October 2011 (Fig. 11a), i.e., we can calculate the rockfall susceptibility after the 2011 collapse and then compare that result against actual rockfall events. In both cases, we found the rockfall sources to be clearly linked to the geometrical characteristics and mechanical behavior of the main structural features.

2010 (pre-failure) susceptibility index and subsequent large-scale failure

In 2010, the areas of highest rockfall susceptibility on the west face of the Drus were two overhanging structures located in the middle of the face (Fig. 11b). This relatively high ranking (about 0.45) is mainly due to the steepest wedges J1-J3, J1-J8, and J2-J8 (Fig. 12b) that have an intersection almost perpendicular with the two overhangs. Thus, the base of the pillar that collapsed in 2011 (Fig. 11a) was in a particularly unstable situation as a consequence of the sub-horizontal overhanging structures and the high probability of failure of the vertical and very persistent wedges. Other important failure mechanisms are the wedges J1-J9 and J8-J9, as well as planar failure along J9 and toppling detachment according to J6, J13, and J14 (Fig. 12).

2011 (post-failure) susceptibility index and subsequent small-scale rockfall activity

We used the point cloud acquired in November 2011 to perform additional susceptibility analysis following the large failures of September–October 2011 (Fig. 11a). By comparing the scan of

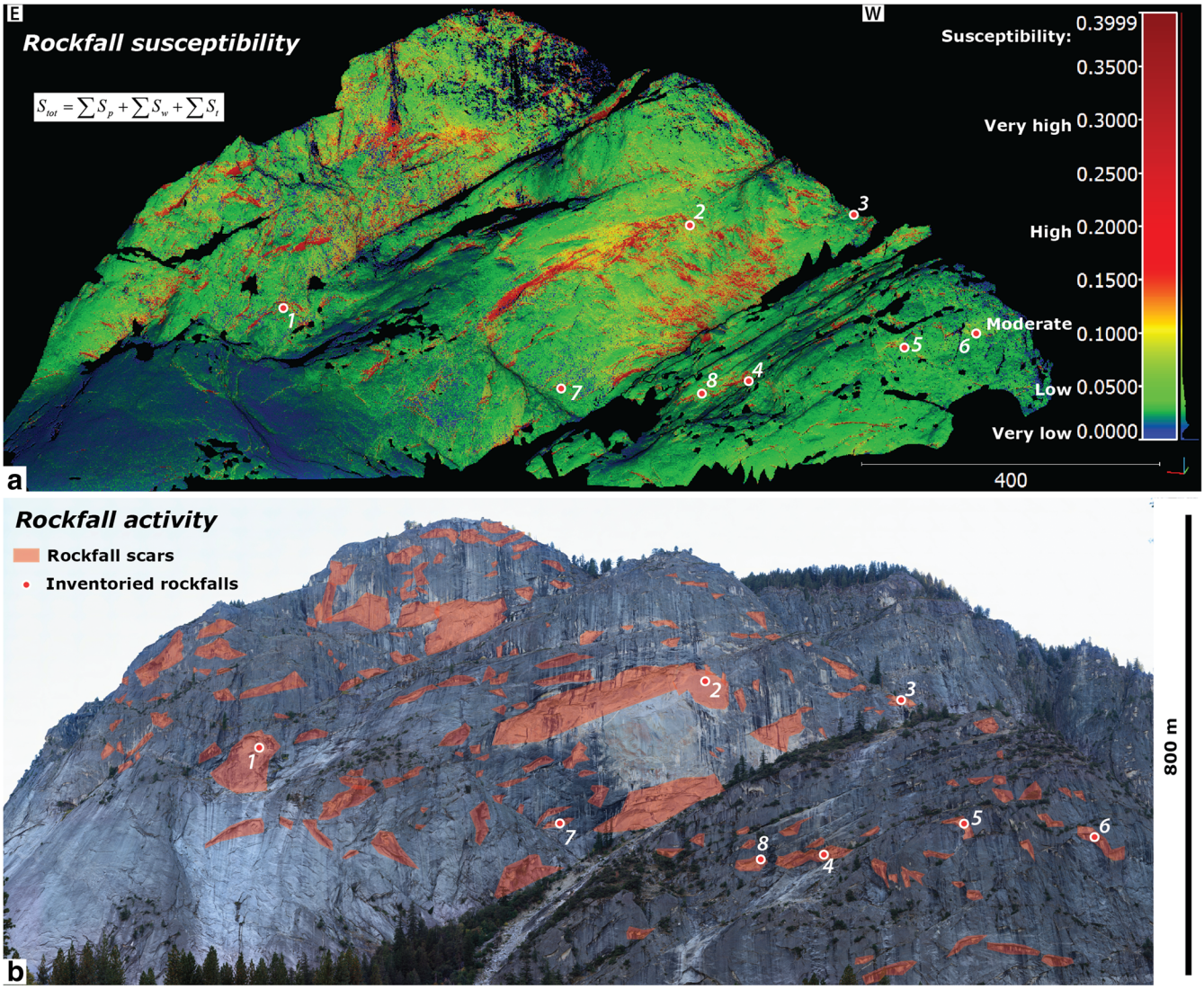

1. 16 Nov. 1998, 563m³
25 May1999, 41m³
13 June 1999, 213m³
15 June 1999, 3m³
17 June 1999, 20m³
14 July 1999, 2m³
14 March 2000, 2m³
14 June 2000, 1m³
29 Aug. 2000, 21m³
10 Oct. 2001, 0.1m³
06 Oct. 2006, 30m³
2012, 1.2m³
2013, 0.14m³

2. 21 Nov. 1985, 20m³
15 Aug. 2001, 13m³
14 Sept. 2001, 60m³
25 Sept. 2001, 6m³
20 July 2003, 16m³
07 Oct. 2008, 1133m³
08 Oct. 2008, 4530m³
03 Sept. 2010, 20m³
01 July 2011, 25m³
2012, 59.1m³

3. 26 Dec. 2003, 204m³
09 June 2007, 18m³

4. 02 Jan. 1997, 2m³

5. 25 Oct. 2005, 144m³
29 Sept. 2009, 55m³

6. 12 Nov. 2011, 13m³
2013, 0.14m³

7. 2012, 0.23m³

8. 2012, 0.14m³

Fig. 9 Comparison between the integrated rockfall susceptibility map and the areas of rockfall activity defined in the field. **a** Point cloud of the rockfall susceptibility calculated by summing the susceptibility index for planar, wedge, and toppling failure (i.e., S_{tot}). **b** GigaPan photograph used to map the visible rockfall scars, shown in red, and the locations of rockfalls that have occurred in the past few decades (numbered red dots), which were documented by eyewitness accounts and field observations (Stock et al. 2013), as well as photographic comparison and several repeat TLS scans between 2007 and 2013 performed as part of this study. Dates with only the year reported identify rockfalls where additional timing information is not known

November 2011 with another data set collected in September 2014, we detected 16 rockfalls, with the largest event having a volume of 132 m³ (Fig. 13a). The most important mechanisms for these rockfalls are the same as for the computation on the 2010 point cloud (Fig. 12), and the most susceptible parts are overhanging structures visible in close-ups 1 and 2 of Fig. 13. Comparison with

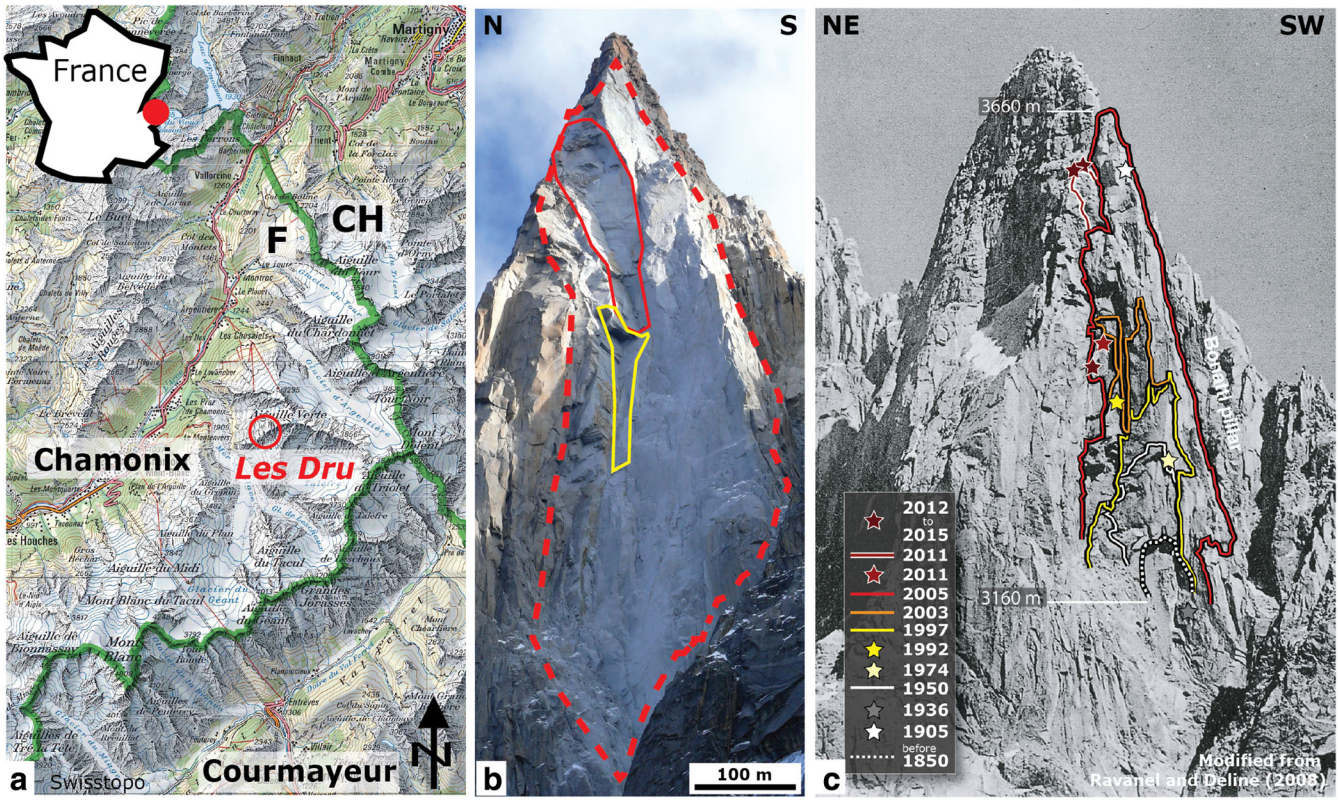

Fig. 10 **a** Setting of the Drus peak within the Mont-Blanc massif (Swisstopo). **b** Present day situation of the west face of the Drus with the scars of the collapses of 2005 (red dashed line) and 2011 (yellow line: September 10–11, Red line: October 29–30). **c** Photo-comparison reconstruction of the main historical rockfalls that occurred in the west face of the Drus (modified from Ravanel and Deline 2008)

the calculated rockfall susceptibility is coherent in most of the cases, as displayed in the close-ups of Fig. 13c–e; in fact, these rockfalls were located directly above zones of high or very high susceptibility.

Table 3 Summary of the characteristics of the joint sets measured with the TLS point cloud in the west face of the Drus

Joint set	Dip direction (°)	Dip (°)	2σ (°)	Spacing (m)	Trace length (m)
J1	238	68	17	6	70
J2	274	84	18	3	80
J3	303	79	17	7	90
J4	065	27	19	7	16
J5	131	8	10	13	15
J6	106	33	22	7	12
J7	029	26	18	8	8
J8	176	80	19	6	40
J9	286	46	17	7	16
J10	211	71	15	15	75
J11	026	81	14	18	60
J12	146	67	14	10	30
J13	058	74	15	11	16
J14	108	66	16	13	17

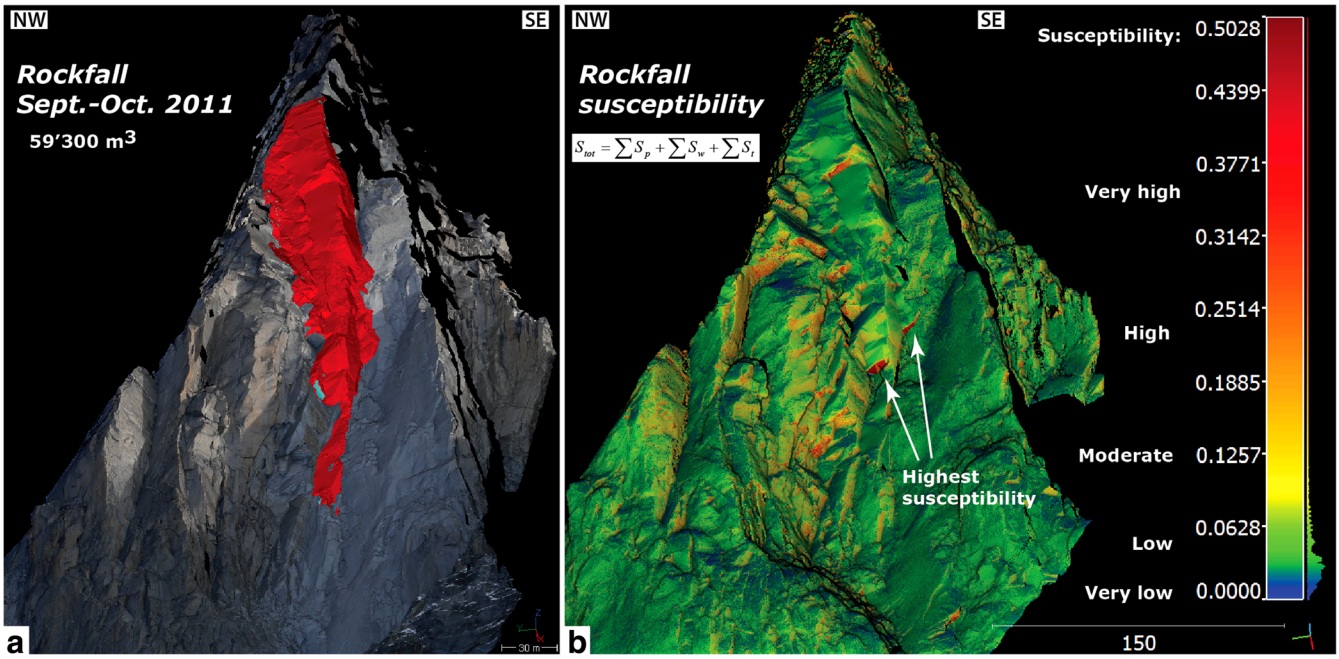

Fig. 11 **a** TLS mesh textured with a photograph displaying the mesh to point comparison between the scans of September 2010 and November 2011. An initial rockfall occurred in September 2011 (4532 ± 200 m^3) close to the base of the pillar, followed by collapse of the entire pillar between 29 and 30 of October (54,731 ± 400 m^3). **b** Result of the susceptibility calculations on the point cloud of 2010, prior to the rockfall events. The arrows indicate two overhanging areas characterized by a particularly high susceptibility rating and located at the base of the collapsed pillar

Discussion

Potential and limits of the susceptibility models

The methods we develop here define the cliff areas with orientations most favorable to failure. The results of this analysis are an additional tool to address the issue of localizing the most probable future rockfall source areas. Both in Yosemite Valley and at the Drus, overhanging areas display the highest rockfall susceptibility indexes, confirming the importance of more accurately analyzing these structures (Figs. 9 and 13). At the Drus, reconstruction of the main historical rockfalls (Fig. 10c) supports these results, demonstrating that rockfall activity propagated toward the top of the face, with successive failures between overhanging structures (Ravanel and Deline 2008).

For both the Glacier Point cliff and the west face of the Drus, our analyses show that most of the inventoried rockfall events occurred in zones with a relatively high rockfall susceptibility index. Of 31 rockfalls documented at these two areas in the past 20 years, approximately 90% of the events took place in relatively high or very high susceptibility areas and only 10% in moderate or low susceptibility areas (Fig. 14).

The values of susceptibility index depend on the characteristics of the discontinuities affecting the studied rock mass, and thus, the definition of low or high susceptibility is relative to the study site. The application sites used in this study have similar rock types and fracturing patterns resulting in comparable, but not directly similar, ranges of rockfall susceptibility. The spatial distribution of the susceptibility index must be interpreted with respect to the values

Fig. 12 Results of susceptibility calculations for **a** planar failure, **b** wedge failure, and **c** toppling detachment mechanism at the west face of the Drus. Joint sets J1-J3, J1-J8, and J2-J8 are particularly susceptible to wedge failure and likely played a major role in the destabilization that resulted in the large failures in September and October 2011

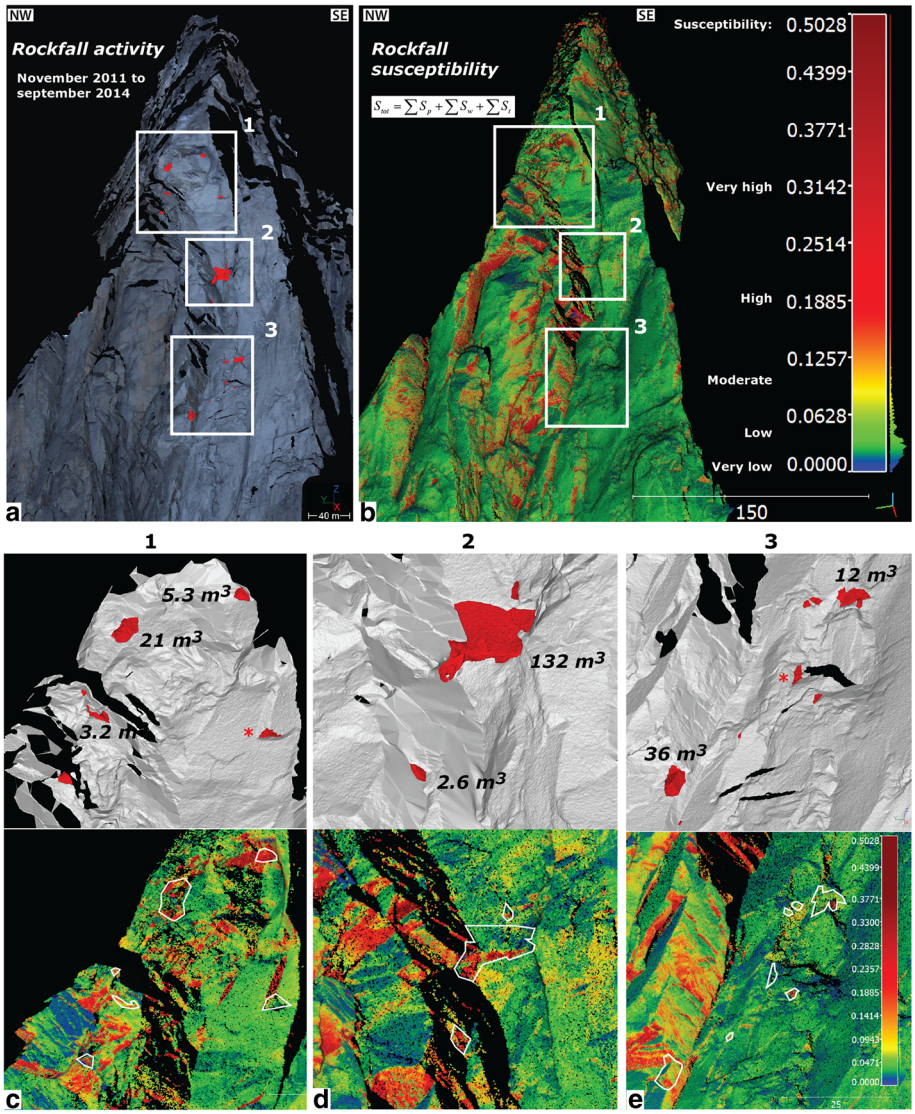

Fig. 13 Comparison between rockfall susceptibility and activity between November 2011 and September 2014 for the Drus west face. **a** Rockfalls detected by mesh to points difference between LiDAR scans. **b** Point cloud showing the computed total rockfall susceptibility (S_{tot}). **c**–**e** The close-ups 1, 2, and 3 (color bar and the scale are identical for **c**–**e**). The rockfalls in close-ups 1 and 3 marked with the asterisk symbol were small, detached flakes lying on low-angle ledges

in the immediate vicinity of the area under investigation and must be compared to the local cliff morphology to assess the dimensions of potential future rockfalls. For instance, a pillar delimited on the sides by vertical joints and at the base by a sub-horizontal joint should be considered as a complete unstable rock mass, even if the points in the vertical facets have a lower susceptibility rating than those in the overhanging part. In fact, it is difficult to reliably determine a priori, at the cliff scale, if only parts of such an unstable area will fall or if it will collapse in a single large rockfall event. To evaluate the precise stability conditions of single compartments, it is necessary to perform detailed field investigations and geomechanical stability modeling (Paronuzzi and Serafini 2009; Tsesarsky and Hatzor 2009; Brideau et al. 2011). Our aim in developing this methodology is to define the zones where rockfalls are particularly likely to detach in order to direct the subsequent detailed analysis, such as site-specific run-out trajectory simulations (Frattini et al. 2008; Gigli et al. 2012).

Starting with such a rockfall source detection, the entire rockfall hazard assessment is both more effective and more reliable when compared to traditional approaches that might consider all steep slopes as equivalent source areas. Fanti et al. (2013) and Gigli et al. (2012) greatly improved the kinematic analysis in steep outcrops. With our work, we defined susceptibility indexes to enhance the detection of the most rockfall prone areas among the vertical and overhanging cliff areas (Figs. 9 and 13). In general, the volumes located above overhanging planes are a priori less stable because of the lack of support at the base. When these overhanging structures also have high susceptibility index, the upper rock masses should be considered the most hazardous portions of the cliff, as they

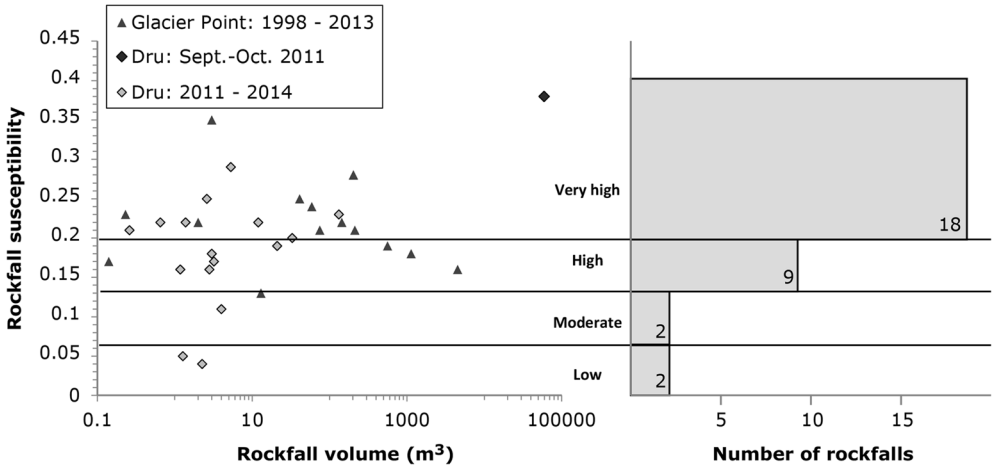

Fig. 14 Total rockfall susceptibility (S_{tot}) for the events that could be located precisely in the west face of the Drus and in the Glacier Point cliff

have a great probability of being detached at the base by daylighting joints or wedges. Thus, our methodology provides a quantitative framework for characterizing these structures.

Comparison of application sites

Although both of our study sites are located in granitic rocks, they have quite distinctive fracturing patterns due to contrasts in pluton ages and tectonic histories. The main structural difference is that, in the Mont-Blanc granite, exfoliation joints are much less frequent. This could be related to the tectonic deformations that it experienced since emplacement (330–320 Ma) and, in particular, during the Alpine orogeny (Bussy and Von Raumer 1994). In contrast, the Cretaceous plutons of the Sierra Nevada underwent less tectonic deformation since emplacement, cooling, and exhumation (Molnar et al. 2007). Moreover, the Drus is situated in a high alpine environment, implying the presence of permafrost, with related weathering, intermittent fluid flow, and ice wedging along joints (Boeckli et al. 2012; Ravanel and Deline 2008; Ravanel et al. 2010; Fischer et al. 2010; Hasler et al. 2012; Krautblatter et al. 2013; Matasci et al. 2015). Finally, the morphologies of the faces are very different because of the joint sets with large trace length. At the Drus, the pervasive structures are the steep wedges that represent the main morphological feature of the west face. At Glacier Point, the most persistent joints are not very steep and dip in opposite directions, perpendicular to the main cliff orientation. For example, J10 is very important for shaping Glacier Point cliff, as the mean orientation of the cliff is sub-parallel to this discontinuity.

Exfoliation failures

Rockfalls in Yosemite Valley are often linked to the propagation of shallow exfoliation joints that are, by definition, parallel to the topography (Wieczorek and Snyder 1999; Stock et al. 2011, 2012). As such, exfoliation joints within a rock mass are hard to resolve with remote sensing methods. As indicated previously, we include the contribution of exfoliation joints to the rockfall susceptibility via the calculation of the planar and toppling susceptibility indexes. The potential for exfoliation failures is included in the toppling susceptibility whenever steep and overhanging slope areas are close to parallel to the regarded joint (Fig. 5). In these cases, the failure is likely to occur in tension. Planar index captures exfoliation where the joint has an oblique intersection with the slope (overhangs; Fig. 5). Where the slope angle is moderate and parallel to the exfoliation joint, the potential of exfoliation failure is probably underestimated because no daylighting of joints occurs and they are therefore not able to be measured for inclusion into the planar susceptibility calculations. The lower portion of the Glacier Point cliff represents a setting where exfoliation joints are parallel to the topographic surface with little to no daylighting or surface expression (Figs. 6b and 9b). Exfoliation joints do exist in this part of the cliff, as they are visible in a few places, and were detected during geophysical investigations in the area (Brody et al. 2015). However, because of the lack of joint expression at the surface, we calculated relatively low rockfall susceptibility in this location (Fig. 9). The calculated low susceptibility at this location may in fact accurately represent the situation, as the low-angle slope and lack of daylighting joints may not allow rock masses to mobilize. In fact, the lower portions of Glacier Point retain glacial polish, indicating that very few rockfalls occurred there since glacial retreat circa 15,000 years ago (Fig. 9). Similarly, the inventory database of Yosemite rockfalls contains relatively few rockfalls from this area (Stock et al. 2013).

At the Rhombus Wall, located across the valley from Glacier Point (see Fig. 6a), a specific area experienced several progressive rockfalls in 2009 and 2010 that detached along exfoliation joints (Stock et al. 2012). In that area, we used terrestrial LiDAR data to measure the spacing between the exfoliation joints. Preliminary results show that the frequency of exfoliation joints is considerably higher in the area of intense rockfall activity, compared to the rest of the cliff. Although the frequency of joints does not provide any indication of the probable failure mechanism, we note that a cliff area with a high frequency of exfoliation joints has a higher probability to produce rockfalls by providing a multitude of potential failure planes that can subsequently slide, topple, or fall. Including additional aspects of exfoliation failures into rockfall susceptibility analyses is a subject for future research.

Conclusions

Application of TLS and high-resolution photographic technologies allowed detailed three-dimensional assessment of the fracturing

pattern of vertical and overhanging cliffs in two distinct rockfall-prone areas. We developed a computation routine of the kinematic failures on terrestrial LiDAR point clouds to assess rockfall susceptibility at the cliff scale. Equations define a susceptibility index for each failure mechanism, according to information accumulated during long-term monitoring of rockfall processes. The susceptibility models obtained for the cliff below Glacier Point (Yosemite Valley) and the west face of the Drus (Mont-Blanc) show a good correspondence with past rockfall sources, demonstrating the validity of the approach. Overhanging areas are found to be important areas requiring detailed study in order to quantify rockfall susceptibility. In Yosemite Valley, the frequency of exfoliation joints plays a central role in the destabilization process contributing to small and medium-sized rockfalls, which are the most common. Most of the effect of exfoliation on rockfall susceptibility is captured by our planar and toppling susceptibility indexes, but assessment of the susceptibility to exfoliation failures remains challenging, in particular where exfoliation joints have no external expression; additional investigations are needed to improve the modeling of this failure mechanism.

The methods we present here for geometrically analyzing in three dimensions the main failure mechanisms potentially acting on a cliff prove to be effective for identifying the most probable future rockfall sources. Calculating the susceptibility of failure can define the points of initiation for future rockfalls. However, temporal forecasting of areas that will fall in the future is still a formidable research challenge. At a minimum, additional geomechanical investigations are needed to define the stability conditions of a specific area. Concerning timing aspects, future research might pursue the improvement of site-specific inventories in order to improve the correlations between rockfall volume and frequency distributions (Dussauge et al. 2003; Guzzetti et al. 2003; Brunetti et al. 2009; Barlow et al. 2012). In both Yosemite Valley and in the Mont-Blanc massif, large efforts have been directed toward this problem, in particular during the past 10 years, with the support of ground based LiDAR (Stock et al. 2012, 2013; Zimmer et al. 2012; Rabatel et al. 2008; Ravanel and Deline 2008, 2011). Coupling susceptibility analysis to frequency distributions of potential rockfall volumes could be the key to improve the effectiveness and reliability of rockfall hazard assessments and to gain new insights on the evolution of steep rocky landscapes.

Acknowledgements

We thank Eric Hanson and Greg Downing of xRez Studio for acquisition of some high-resolution panoramic images of Yosemite Valley.

Funding informationThe authors acknowledge the Swiss National Science Foundation (grants: 146426 and 127132), the US National Park Service, and the US Geological Survey for supporting this research.

References

Abellan A, Vilaplana JM, Calvet J, Blanchard J (2010) Detection and spatial prediction of rockfalls by means of terrestrial laser scanning modelling. Geomorphology 119:162–171

Abellan A, Oppikofer T, Jaboyedoff M, Rosser NJ, Lim M, Lato MJ (2014) Terrestrial laser scanning of rock slope instabilities. Earth Surf Process Landforms 39:80–97

Aksoy H, Ercanoglu M (2006) Determination of the rockfall source in an urban settlement area by using a rule-based fuzzy evaluation. NHESS 6:941–954

Bahat, D., Grossenbacher, K., And Karasaki, K., 1999. Mechanism of exfoliation joint formation in granitic rocks, Yosemite National Park. J Struct Geol, 21, 85–96

Baillifard F, Jaboyedoff M, Sartori M (2003) Rockfall hazard mapping along a mountainous road in Switzerland using a GIS-based parameter rating approach. NHESS 3:435–442

Barlow J, Lim M, Rosser N, Petley D, Brain M, Norman E, Geer M (2012) Modeling cliff erosion using negative power law scaling of rockfalls. Geomorphology 139:416–424

Bateman PC (1992) Plutonism in the central part of the Sierra Nevada batholith, California (No.1483)

Besl P, Mckay N (1992) A method for registration of 3-d shapes. IEEE Trans Pattern Anal Mach Intell 14:239–256

Bieniawski ZT (1973) Engineering classification of jointed rock masses. Civil Engineer in South Africa 15(12)

Bieniawski ZT (1979) The geomechanics classification in rock engineering applications, ISRM Montreux, Proc. 4th Int. Cong. on Rock Mech., Balkema, Rotterdam, pp 55–95

Boeckli L, Brenning A, Gruber S, Noetzli J (2012) Permafrost distribution in the European Alps: calculation and evaluation of an index map and summary statistics. Cryosphere 6:807–820. https://doi.org/10.5194/tc-6-807-2012

Brideau MA, Pedrazzini A, Stead D, Froese C, Jaboyedoff M, van Zeyl D (2011) Three-dimensional slope stability analysis of South Peak, Crowsnest Pass, Alberta, Canada. Landslides 8(2):139–158

Brody AG, Pluhar CJ, Stock GM, Greenwood WJ (2015) Near-surface geophysical imaging of a talus deposit in Yosemite Valley, California. Environ Eng Geosci 21(2):111–127

Brunetti MT, Guzzetti F, Rossi M (2009) Probability distributions of landslide volumes. Nonlinear Process Geophys 16(2):179–188

Bussy F, Von Raumer J (1994) U–Pb geochronology of Palaeozoic magmatic events in the Mont-Blanc Crystalline Massif, Western Alps. Schweizerische Mineralogische Petrographische Mitteilungen 74:514–515

Calkins FC, Huber NK, Roller JA (1985) Geologic bedrock map of Yosemite Valley, Yosemite National Park, California. US Geol Surv, Map I-1639

Chen Y, Medioni G (1992) Object modelling by registration of multiple range images. Image Vis Comput 10:145–155. https://doi.org/10.1016/0262-8856(92)90066-C

Collins B, Sitar N (2008) Processes of coastal bluff erosion in weakly lithified sands, Pacifica, California, USA. Geomorphology 97:483–501

Collins BD, Stock GM (2016) Rockfall triggering by cyclic thermal stressing of exfoliation fractures. Nat Geosci 9:395–400. https://doi.org/10.1038/ngeo2686

Copons R, Vilaplana JM (2008) Rockfall susceptibility zoning at a large scale: from geomorphological inventory to preliminary land use planning. Eng Geol 102(3):142–151

Crosta GB, Agliardi F (2003) A new methodology for physically based rockfall hazard assessment. Nat Hazards Earth Syst Sci 3:407–422

Deline P et al (2006) Permafrost and rock falls in high mountain: the Drus (Mont Blanc massif, France). Geophys Res Abstr 8:02033

Dershowitz WS, Einstein HH (1988) Characterizing rock joint geometry with joint system models. Rock Mech Rock Eng 21:21–51

Dorren LKA, Seijmonsbergen AC (2003) Comparison of three GIS-based models for predicting rockfall runout zones at a regional scale. Geomorphology 56(1–2):49–64

Dunham L, Wartman J, Olsen MJ, O'Banion M, Cunningham K (2017) Rockfall Activity Index (RAI): a lidar-derived, morphology-based method for hazard assessment. Eng Geol 221:184–192

Dussauge C, Grasso JR, Helmstetter A (2003) Statistical analysis of rockfall volume distributions: Implications for rockfall dynamics. J Geophys Res Solid Earth 108(B6). https://doi.org/10.1029/2001JB000650

Eberhardt E (2003) Rock slope stability analysis–utilization of advanced numerical techniques. Earth and Ocean sciences at UBC

Einstein HH (1988) Special lecture: landslide risk assessment procedure. MIT, USA, pp 1075–1090

Epard JL (1990) La nappe de Morcles au sud-ouest du Mont-Blanc (Doctoral dissertation, Université de Lausanne)

Evans SG, Hungr O (1993) The assessment of rockfall hazard at the base of talus slopes. Can Geotech J 30(4):620–636

Fanti R, Gigli G, Lombardi L, Tapete D, Canuti P (2013) Terrestrial laser scanning for rockfall stability analysis in the cultural heritage site of Pitigliano (Italy). Landslides 10(4):409–420

Ferrero AM, Forlani G, Roncella R, Voyat HI (2009) Advanced geostructural survey methods applied to rock mass characterization. Rock Mech Rock Eng 42:631–665

Fischer L, Amann F, Moore JR, Huggel C (2010) Assessment of periglacial slope stability for the 1988 Tschierva rock avalanche (Piz Morteratsch, Switzerland). Eng Geol 116(1):32–43

Frattini P, Crosta G, Carrara A, Agliardi F (2008) Assessment of rockfall susceptibility by integrating statistical and physically-based approaches. Geomorphology 94:419–437
Gigli G, Casagli N (2011) Semi-automatic extraction of rock mass structural data from high resolution LIDAR point clouds. Int J Rock Mech Min Sci 48(2):187–198
Gigli G, Morelli S, Fornera S, Casagli N (2012) Terrestrial laser scanner and geomechanical surveys for the rapid evaluation of rock fall susceptibility scenarios. Landslides:1–14. https://doi.org/10.1007/s10346-012-0374-0
Gischig V, Amann F, Moore JR, Loew S, Eisenbeiss H, Stempfhuber W (2011) Composite rock slope kinematics at the current Randa instability, Switzerland, based on remote sensing and numerical modeling. Eng Geol 118:37–53
Gokceoglu C, Sonmez H, Ercanoglu M (2000) Discontinuity controlled probabilistic slope failure risk maps of the Altindag (settlement) region in Turkey. Eng Geol 55:277–296
Goodman RE & Bray JW (1976) Toppling of rock slopes. ASCE Specialty Conference on Rock Engineering for Foundations and Slopes, Boulder Colorado 2:201–234
Goodman RE, Shi GH (1985) Block theory and its application to rock engineering. Prentice-Hall, Englewood Cliffs
Grenon M, Hadjigeorgiou J (2008) A design methodology for rock slopes susceptible to wedge failure using fracture system modelling. Eng Geol 96:78–93
Guenther A, Carstensen A, Pohl W (2004) Automated sliding susceptibility mapping of rock slopes. Nat Hazards Earth Syst Sci 4:95–102
Guenther A, Wienhöfer J, Konietzky H (2012) Automated mapping of rock slope geometry, kinematics and stability with RSS-GIS. Nat Hazards 61(1):29–49
Guérin A, Abellán A, Matasci B, Jaboyedoff M, Derron M-H, and Ravanel L (2017) Brief communication: 3D reconstruction of a collapsed rock pillar from web-retrieved images and terrestrial LiDAR data—the 2005 event of the West face of the Drus (Mont-Blanc massif). Nat Hazards Earth Syst Sci Discuss in review.https://doi.org/10.5194/nhess-2016-316
Guzzetti F, Reichenbach P, Wieczorek GF (2003) Rockfall hazard and risk assessment in the Yosemite Valley, California, USA. NHESS 3:491–503
Hales T. C., And Roering J. J., (2007), Climatic controls on frost cracking and implications for the evolution of bedrock landscapes, Journal of Geophysical Research, 112, F02033, https://doi.org/10.1029/2006JF000616
Harp EL, Noble MA (1993) An engineering rock classification to evaluate seismic rock-fall susceptibility and its application to the Wasatch Front. Bull Assoc Eng Geol 30(3)
Hasler A, Gruber S, Beutel J (2012) Kinematics of steep bedrock permafrost. J Geophys Res Earth Surf 117(F1). https://doi.org/10.1029/2011JF001981
Hoek E, Bray JW (1981) Rock slope engineering, 3rd edn. Institution of Mining and Metallurgy, London
Huber NK (1987) The geologic story of Yosemite National Park (No. 1595). USGPO, Washington, D.C
Hudson JA, Priest SD (1983) Discontinuity frequency in rock masses. Int J Rock Mech Min Sci Geomech Abstr 20(2):73–89
Humair F, Pedrazzini A, Epard JL, Froese CR, Jaboyedoff M (2013) Structural characterization of Turtle Mountain anticline (Alberta, Canada) and impact on rock slope failure. Tectonophysics 605:133–148
Hungr O, Evans S, Hazzard J (1999) Magnitude and frequency of rock falls along the main transportation corridors of south-western British Columbia. Can Geotech J 36:224–238
Irigaray C, Fernández T, Chacón J (2003) Preliminary rock-slope-susceptibility assessment using GIS and the SMR classification. Nat Hazards 30(3):309–324
ISRM (1978) Suggested methods for the quantitative description of discontinuities in rock masses. Int J Rock Mech Min Sci 15:319–368. https://doi.org/10.1016/0148-9062(78)91472-9
Jaboyedoff M, Philippossian F, Mamin M, Carro C and Rouiller J-D (1996) Distribution spatiale des discontinuités dans une falaise, Cahier du PNR31, VDF 90 pp
Jaboyedoff M, Baillifard F, Philippossian F, Rouiller JD (2004) Assessing fracture occurrence using weighted fracturing density: a step towards estimating rock instability. Nat Hazards Earth Syst Sci 4:83–93
Jaboyedoff M, Metzger R, Oppikofer T, Couture R, Derron M-H, Locat J, Turmel D (2007) New insight techniques to analyze rock-slope relief using DEM and 3D–imaging cloud points: COLTOP-3Dsoftware. Proceedings of the 1st Canada–U.S. Rock Mechanics Symposium
Jaboyedoff M, Couture R, Locat P (2009) Structural analysis of Turtle Mountain (Alberta) using digital elevation model: toward a progressive failure. Geomorphology 103(1):5–16
Jaboyedoff M, Oppikofer T, Abellán A, Derron MH, Loye A, Metzger R, Pedrazzini A (2012) Use of LIDAR in landslide investigations: a review. Nat Hazards 61(1):5–28
Krautblatter M, Funk D, Günzel FK (2013) Why permafrost rocks become unstable: a rock–ice-mechanical model in time and space. Earth Surf Process Landf 38(8):876–887
Lato M, Vöge M (2012) Automated mapping of rock discontinuities in 3D lidar and photogrammetry models. Int J Rock Mech Min Sci 54:150–158
Lato M, Diederichs MS, Hutchinson DJ, Harrap R (2009) Optimization of LIDAR scanning and processing for automated structural evaluation of discontinuities in rockmasses. Int J Rock Mech Min Sci 46:194–199
Lato MJ, Diederichs MS, Hutchinson DJ (2012) Evaluating roadside rockmasses for rockfall hazards using LiDAR data: optimizing data collection and processing protocols. Nat Hazards 60:831–864
Leith K, Moore JR, Amann F, Loew S (2014) In situ stress control on microcrack generation and macroscopic extensional fracture in exhuming bedrock. J Geophys Res Solid Earth 119:594–615. https://doi.org/10.1002/2012JB009801
Loye A, Jaboyedoff M and Pedrazzini A (2009) Identification of potential rockfall source areas at regional scale using a DEM-based quantitative geomorphometric analysis. NHESS In Review
Markland JT (1972) A useful technique for estimating the stability of rock slope when the rigid wedge sliding type of failure is expected, rock mechanics research report 19. Imperial College London, London
Martel SJ (2006) Effect of topographic curvature on near-surface stresses and application to sheeting discontinuities. Geophys Res Lett 33:L01308
Martel SJ (2011) Mechanics of curved surfaces, with application to surface-parallel cracks. Geophys Res Lett 38(L20303). https://doi.org/10.1029/ 2011GL049354
Matasci B, Jaboyedoff M, Ravanel L, Deline P (2015) Stability assessment, potential collapses and future evolution of the west face of the Drus (3,754 m a.s.l., Mont Blanc Massif). In: Lollino G et al (eds) Engineering Geology for Society and Territory—volume 2. © Springer International Publishing, Switzerland. https://doi.org/10.1007/978-3-319-09057-3_134
Matsuoka N, Sakai H (1999) Rockfall activity from an alpine cliff during thawing periods. Geomorphology 28:309–328
Mazzoccola DF, Hudson JA (1996) A comprehensive method of rock mass characterization for indicating natural slope instability. Q J Eng Geol Hydroge 29:37
Messenzehl K, Meyer H, Otto J-C, Hoffmann T, Dikau R (2016) Regional-scale controls on the spatial activity of rockfalls (Turtmann Valley, Swiss Alps)—a multivariate modeling approach. Geomorphology. Available online 22 January 2016, ISSN 0169-555X. https://doi.org/10.1016/j.geomorph.2016.01.008
Michoud C., Derron M.-H., Horton P., Jaboyedoff M., Baillifard F.-J., Loye A., Nicolet P., Pedrazzini A., And Queyrel A., (2012), Rockfall hazard and risk assessments along roads at a regional scale: example in Swiss Alps, Nat Hazards Earth Syst Sci, 12, 615–629, https://doi.org/10.5194/nhess-12-615-2012
Molnar P, Anderson RS, Anderson SP (2007) Tectonics, fracturing of rock, and erosion. J Geophys Res Earth Surf 112:F3. https://doi.org/10.1029/2005JF000433
Moore JR, Sanders JW, Dietrich WE, Glaser SD (2009) Influence of rockmass strength on the erosion rate of alpine cliffs. Earth Surf Process Landf 34:1339–1352
Nex F, Remondino F (2014) UAV for 3D mapping applications: a review. Appl Geomatics 6(1):1–15
Niethammer U, James MR, Rothmund S, Travelletti J, Joswig M (2012) UAV-based remote sensing of the Super-Sauze landslide: evaluation and results. Eng Geol 128:2–11
Norrish N, Wyllie D (1996) Rock slope stability analysis, in landslides investigation and mitigation. In: Turner K, Schuster R (eds) Transportation Research Board Special Report 247. National Academy Press, Washington D.C., pp 391–425
Oppikofer T, Jaboyedoff M, Keusen HR (2008) Collapse at the eastern Eiger flank in the Swiss alps. Nat Geosci 1:531–535. https://doi.org/10.1038/ngeo258
Oppikofer T, Jaboyedoff M, Pedrazzini A, Derron M-H, Blikra L (2011) Detailed DEM analysis of a rockslide scar to characterize the basal sliding surface of active rockslides. J Geophys Res 116:22
Paronuzzi P, Serafini W (2009) Stress state analysis of a collapsed overhanging rock slab: a case study. Eng Geol 108(2009):65–75. https://doi.org/10.1016/j.enggeo.2009.06.019
Peck D (2002) Geologic map of the Yosemite quadrangle, central sierra Nevada, California, U.S. Geol Surv Geol Investig Ser Map I-2751, scale 1:62,500
Priest SD (1993) Discontinuity analysis for rock engineering. Chapman and Hall, London 473 pp
Rabatel A, Deline P, Jaillet S, Ravanel L (2008) Rock falls in high-alpine rock walls quantified by terrestrial lidar measurements: a case study in the Mont Blanc area. Geophys Res Lett 35:L10502
Ravanel L, Deline P (2008) La face ouest des Drus (massif du Mont-Blanc): évolution de l'instabilité d'une paroi rocheuse dans la haute montagne alpine depuis la fin du petit âge glaciaire. Géomorphologie: Relief, Processus, Environnement 14(4):261–272
Ravanel L, Deline P (2011) Climate influence on rockfalls in high-Alpine steep rockwalls: the north side of the Aiguilles de Chamonix (Mont Blanc massif) since the end of the 'Little Ice Age'. The Holocene 21(2):357–365

Ravanel L, Allignol F, Deline P, Gruber S, Ravello M (2010) Rock falls in the Mont Blanc Massif in 2007 and 2008. Landslides 7(4):493–501

Riquelme AJ, Abellán A, Tomás R, Jaboyedoff M (2014) A new approach for semi-automatic rock mass joints recognition from 3D point clouds. Comput Geosci 68:38–52

Romana M (1985) New adjustment ratings for application of Bieniawski classification to slopes. Proceedings of Int. Symp. Role of Rock Mech., ISRM, Zacatecas, pp 49–53

Romana M (1993) A geomechanical classification for slopes: slope mass rating. Comprehensive rock engineering 3(1):575–599

Rosser NJ, Lim N, Petley DN, Dunning S, Allison RJ (2007) Patterns of precursory rockfall prior to slope failure. J Geophys Res 112(F4). https://doi.org/10.1029/2006JF000642

Royan MJ, Abellán A, Jaboyedoff M, Vilaplana JM, Calvet J (2014) Spatio-temporal analysis of rockfall pre-failure deformation using terrestrial LiDAR. Landslides 11(4):697–709

Selby MJ (1982) Controls on the stability and inclinations of hillslopes formed on hard rock. Earth Surf Proc Land 7:449–467

Slob S, Hack R (2004) 3D terrestrial laser scanning as a new field measurement and monitoring technique. In: Engineering geology for infrastructure planning in Europe: a European perspective, Lectures Notes in Earth Sciences, Springer, Berlin/Heidelberg 104:179–189

Stead D, Wolter A (2015) A critical review of rock slope failure mechanisms: the importance of structural geology. J Struct Geol 74:1–23

Steck A, Bigioggero B, Dal Piaz GV, Escher A, Martinotti G, & Masson H (1999) Carte tectonique des Alpes de Suisse occidentale et des régions avoisinantes 1:100'000. In Carte géologique spéciale (Vol. 123). Bern: Service hydrologique et géologique national

Stock GM, and Uhrhammer RA (2010) Catastrophic rock avalanche 3600 years B.P. from El Capitan, Yosemite Valley, California, Earth Surface Processes and Landforms 35:941–951

Stock GM, Bawden GW, Green JK, Hanson E, Downing G, Collins BD, Bond S, Leslar M (2011) High-resolution three-dimensional imaging and analysis of rock falls in Yosemite Valley, California. Geosphere 7:573–581

Stock GM, Martel SJ, Collins BD, Harp EL (2012) Progressive failure of sheeted rock slopes: the 2009-2010 Rhombus Wall rock falls in Yosemite Valley, California, USA. Earth Surf Process Landforms 37:546–561

Stock GM, Collins BD, Santaniello DJ, Zimmer VL, Wieczorek GF, Snyder JB (2013) Historical rock falls in Yosemite National Park (1857–2011). U.S. Geological Survey Data Series 746

Stock GM, Luco N, Collins BD, Harp EL, Reichenbach P, Frankel KL (2014) Quantitative rock-fall hazard and risk assessment for Yosemite Valley, Yosemite National Park, California. U.S Geological Survey Scientific Investigatoins Report 2014-5129, 52 p. http://www.pubs.usgs.gov/sir/2014/5129/

Strahler AN (1954) Quantitative geomorphology of erosional landscapes. Compt Rend 19th Intern Geol Cong, Sec 13:341–354

Sturzenegger M, Stead D (2009) Close-range terrestrial digital photogrammetry and terrestrial laser scanning for discontinuity characterization on rock cuts. Eng Geol 106:163–182

Sturzenegger M, Stead D, Elmo D (2011) Terrestrial remote sensing-based estimation of mean trace length trace intensity and block size/shape. Eng Geol 119(3–4):96–111. https://doi.org/10.1016/j.enggeo.2011.02.005

Terzaghi K (1962) Stability of slopes on hard unweathered rock. Geotechnique 12:251–263

Tsesarsky M, Hatzor YH (2009) Kinematics of overhanging slopes in discontinuous rock. J Geotech Geoenviron Eng 135:1122–1129. https://doi.org/10.1061/ASCEGT.1943-5606.0000049

Vangeon J-M, Hantz D, Dussauge C (2001) Rockfall predictibility: a probabilistic approach combining historical and geomechanical studies. Revue Française de Gotechnique 95(96):143–154

Varnes DJ (1978) Slope movements: types and processes. In: Schuster RL, Krizek RJ (eds) Landslide analysis and control. Transportation Research Board, Special Report No. 176, Washington, DC, pp 11–33

Voege M, Lato MJ, Diederichs MS (2013) Automated rockmass discontinuity mapping from 3-dimensional surface data. Eng Geol 164:155–162

Wickens EH, Barton NR (1971) The application of photogrammetry to the stability of excavated rock slopes. Photogram Rec 7(37):46–54

Wieczorek GF, Snyder JB (1999) Rock falls from Glacier Point above Camp Curry, Yosemite National Park, California, U.S. Geological Survey Open-File Report 99–385. http://pubs.usgs.gov/of/1999/ofr-99-0385/

Wieczorek GF, Stock GM, Reichenbach P, Snyder JB, Borchers JW, Godt JW (2008) Investigation and hazard assessment of the 2003 and 2007 staircase falls rock falls, Yosemite National Park, California, USA. Nat Hazards Earth Syst Sci 8:421–432

Wyllie DC, Mah C (2004) Rock slope engineering. CRC Press

Zimmer V, Collins BD, Stock GM, Sitar N (2012) Rock fall dynamics and deposition: an integrated analysis of the 2009 Ahwiyah Point rock fall, Yosemite National Park, USA. Earth Surf Process Landf 37(6):680–691

B. Matasci (✉) · **M. Jaboyedoff** · **D. Carrea** · **A. Guérin**
Institute of Earth Sciences,
University of Lausanne,
Lausanne, Switzerland
Email: battista.matasci@gmail.com

G. M. Stock
National Park Service,
Yosemite National Park, El Portal, CA 95318, USA

B. D. Collins
Landslide Hazard Program,
U.S. Geological Survey,
Menlo Park, CA 94025, USA

G. Matasci
Institute of Earth Surface Dynamics,
University of Lausanne,
Lausanne, Switzerland

L. Ravanel
EDYTEM,
University of Savoie,
Chambery, France